



저작자표시-비영리-변경금지 2.0 대한민국

이용자는 아래의 조건을 따르는 경우에 한하여 자유롭게

- 이 저작물을 복제, 배포, 전송, 전시, 공연 및 방송할 수 있습니다.

다음과 같은 조건을 따라야 합니다:



저작자표시. 귀하는 원저작자를 표시하여야 합니다.



비영리. 귀하는 이 저작물을 영리 목적으로 이용할 수 없습니다.



변경금지. 귀하는 이 저작물을 개작, 변형 또는 가공할 수 없습니다.

- 귀하는, 이 저작물의 재이용이나 배포의 경우, 이 저작물에 적용된 이용허락조건을 명확하게 나타내어야 합니다.
- 저작권자로부터 별도의 허가를 받으면 이러한 조건들은 적용되지 않습니다.

저작권법에 따른 이용자의 권리는 위의 내용에 의하여 영향을 받지 않습니다.

이것은 [이용허락규약\(Legal Code\)](#)을 이해하기 쉽게 요약한 것입니다.

[Disclaimer](#)

공학박사학위논문

**팩인홀 작업을 위한 다자유도 그리퍼 및
각도 에러 측정 시스템의 설계**

**Design of A Dexterous Gripper with An Angular Error
Measurement System for Peg-In-Hole Task**

2017 년 8 월

서울대학교 대학원

기계항공공학부

김 전 우

Abstract

Peg-In-Hole is the one of basic tasks for robotic assembly. For successful Peg-In-Hole, the position and orientation alignment between mating parts is very important because small error can induce jamming and wedging which generates excessive force leading to damages on mating parts during insertion. A lot of researches for Peg-In-Hole task have been underway and it can be categorized into passive and active approaches. The passive approach represented by Remote Center Compliance uses the compliance and shape of mating parts for alignment, whereas the active approach uses measurement from vision, force or both of them. Passive approach has strength in which alignment can be done passively without any other measurements but applications are limited because it depends on the shape of mating parts like chamfer size and length of peg. Utilization of vision is also limited because of sensitivity in accuracy which is affected significantly by camera location and surrounding environment.

In this dissertation, a dexterous gripper with an angular error measuring instrument and reliable position error estimation algorithm by clustering the force dataset is proposed for Peg-In-Hole task. Three main key features stated below are implemented in the system design and tested with square Peg-In-Hole experiments.

The dexterous gripper which consists of 4 DOF(Degree Of Freedom) two fingers embedded with 6 axis force sensors at the fingertip is designed for micro manipulation during error recovery. Unlike the usual method in which force sensor is mounted on the robot wrist and peg is manipulated by robot arm, the designed dexterous gripper is used for both of grasping and manipulating peg. Reaction force generated on both side of peg is also measured at fingertip and recorded with peg position for error estimation.

Robust angle measuring instrument, Scanner, consisted of 2DOF manipulator and laser distance sensor is also designed and implemented for detecting the angular error between peg and hole. Depending on the contact condition, it's decided whether moment is generated or not, thus angular error compensation is necessary for fast and reliable error estimation based on the force data. In case of square Peg-In-Hole, the

contact condition can be classified into 5 cases depending on the number of edge and supporting area between peg and hole and moment is generated in only one case. With the angular error compensation, the number of contact condition can be diminished to 2 cases thus shortened recovery time can be accomplished.

To extract the position error between peg and hole, error estimation with clustering algorithm is applied to the measured dataset of moment and peg position. Even after angular error compensation, there still exists the condition which generates no reaction moment, thus artificial intelligence which can extract the position error among mixed dataset is required. Two representative algorithms, K means algorithms and Gaussian Mixture Model algorithm, commonly used in machine learning for clustering dataset are applied to various datasets constructed with position and moment for estimating position error. Two datasets, one constructed with the three datasets measured at same condition and the other constructed with three datasets measured with different velocity are used to check accuracy and robustness in error estimation from both of algorithm. The accuracy of estimated position error and deviation among estimated error in each dataset from K means algorithm is within 0.29mm and 0.14mm whereas both of that from Gaussian Mixture Model algorithm is within 0.44mm and 0.43mm. K means algorithm shows stable accuracy and robustness on position error estimation whereas the Gaussian Mixture Model algorithm needs to use constrained parameter for both of them.

Comparing with blind search which uses no information from sensors and long spiral trajectory for error recovery, the proposed measurement system and algorithms have advantages in terms of recovery time and no variation of it. Short XY trajectory which moves horizontally and vertically in given search area can be used and error recovery time have no variation regardless of position error by diminishing the number of contact conditions through angular error compensation.

Keywords: Robotic Assembly, Peg-In-Hole Task, Error Recovery Algorithm, Blind Search, Intelligent search, Dexterous Gripper

Student Number: 2014-30339

Index for Contents

| | |
|---|-----------|
| Abstract | I |
| Chapter 1. Introduction | 1 |
| 1.1. Robotic Assembly and Peg-In-Hole Task | 1 |
| 1.2. Previous Research Works | 2 |
| 1.2.1. Passive approaches | 3 |
| 1.2.2. Active approaches | 5 |
| 1.3. Purpose and Contribution of Research | 9 |
| Chapter 2. Contact Condition Analysis | 12 |
| 2.1. Classification of Contact Condition | 12 |
| 2.1.1. Connected Component Labeling | 12 |
| 2.1.2. Binary image generation procedure | 13 |
| 2.1.3. Analysis results for contact condition | 14 |
| 2.2. Force and Moment depending on Contact Condition | 17 |
| Chapter 3. Design Synthesis of Gripper and Scanner | 21 |
| 3.1. Overall Design Overview | 21 |
| 3.2. Design and Mechanism of Finger | 23 |
| 3.2.1. Advantages of parallel mechanism | 23 |
| 3.2.2. Mechanism description of finger | 28 |
| 3.2.3. Kinematics of finger | 31 |
| 3.3 Design and Mechanism of Scanner | 33 |
| 3.3.1. Mechanism description | 33 |
| 3.3.2. FEM analysis for deflection compensation | 34 |

| | |
|---|-----------|
| Chapter 4. Error Recovery Algorithms | 40 |
| 4.1. Clustering for Error Estimation | 40 |
| 4.1.1. K means algorithm | 41 |
| 4.1.2. Gaussian Mixture Model algorithm | 42 |
| 4.2. Procedure for Error Recovery | 44 |
| 4.3. Comparison of Error Recovery Algorithms | 45 |
| 4.3.1. Comparison of trajectory in blind and XY search | 45 |
| 4.3.2. Comparison of trajectory for position error recovery | 46 |
| 4.3.3. Comparison of trajectory for angular error recovery | 49 |
| 4.3.4. Comparison of variation in recovery time | 50 |
| Chapter 5. Experimental Results | 52 |
| 5.1. Angular Error Measurement of Scanner | 52 |
| 5.1.1. Verification of scanner accuracy and repeatability | 52 |
| 5.1.2. Measurement and alignment of angular error | 56 |
| 5.2. Reaction Moment Measurement at Fingertip | 58 |
| 5.2.1. Measurement of moment data | 58 |
| 5.2.2. Description of measurement condition | 59 |
| 5.2.3. Clustering results from K means algorithm | 61 |
| 5.2.4. Clustering results from Gaussian Mixture Model Algorithm | 64 |
| 5.2.5 Comparison of clustering result | 69 |
| Chapter 6. Conclusion | 71 |
| Bibliography | 74 |
| Abstract in Korean | 78 |

List of the Tables

| | | |
|-----------|---|----|
| Table 2.1 | Number of contact conditions in each case depending on the angular error | 16 |
| Table 2.2 | Summary of reaction force determined from contact condition | 20 |
| Table 3.1 | Natural frequency of cantilevered aluminum frame | 39 |
| Table 4.1 | Trajectory comparison of Blind Search and XY Search for position error recovery | 47 |
| Table 4.2 | Trajectory comparison of Blind Search and XY Search when search distance and clearance is same in height and length | 48 |
| Table 4.3 | Trajectory comparison of Blind Search and XY Search with given search distance and clearance | 48 |
| Table 4.4 | Trajectory comparison of Blind Search and XY Search for angular error compensation | 50 |
| Table 4.5 | Variation of recovery time in Blind Search and XY Search for position error compensation | 51 |
| Table 5.1 | Accuracy, repeatability and worst-case deviation of scanner measurement | 54 |
| Table 5.2 | Measurement error of scanner | 55 |
| Table 5.3 | Analysis result for measurement error | 55 |
| Table 5.4 | Clustering results with k means algorithm on three datasets measured from same condition | 62 |
| Table 5.5 | Clustering results with k means algorithm on three datasets measured from different velocity | 64 |
| Table 5.6 | Clustering results with gaussian mixtue model algorithm on three datasets measured from same condition | 67 |
| Table 5.7 | Clustering results with gaussian mixtue model algorithm on three datasets measured from different velocity | 69 |

List of the Figures

| | | |
|------------|--|----|
| Figure 1.1 | Conditions for Jamming and Wedging | 2 |
| Figure 1.2 | Classification of aligning way | 3 |
| Figure 1.3 | Principle of RCC from ATI Industrial Automation | 4 |
| Figure 1.4 | VRCC mechanism with electromagnet [5] (Left) and ESP modulation [7] (Right) | 4 |
| Figure 1.5 | Blind search for square Peg-In-Hole [14] | 5 |
| Figure 1.6 | Intelligent search algorithm with shape recognition [19, 20] | 6 |
| Figure 1.7 | Fault detection model during connector insertion [15] | 7 |
| Figure 1.8 | Peg-In-Hole based on vision with high speed camera [25] (Left) and IPMC gripper [24] (Right) | 8 |
| Figure 1.9 | Complex shaped part assembly with force and vision information [30, 36] | 9 |
| Figure 2.1 | Example of connected component labeling (Top) and results with different connectivity (Bottom) | 13 |
| Figure 2.2 | Binary image generation procedures for Connected Component Labeling | 14 |
| Figure 2.3 | Five contact conditions in square Peg-In-Hole | 15 |
| Figure 2.4 | Distribution of five contact conditions in square Peg-In-Hole | 17 |
| Figure 2.5 | Moment generation with respect to contact condition | 18 |
| Figure 2.6 | Center position estimation from Connected Component Labeling ... | 18 |
| Figure 2.7 | Reaction force and moment at the finger | 19 |
| Figure 3.1 | Schematics and specification of finger and scanner | 22 |
| Figure 3.2 | Prototype and schematics of electronics hardware | 23 |
| Figure 3.3 | Articulated robot arm with serial structure | 25 |
| Figure 3.4 | Effective mass depending on the position of end effector | 25 |

| | | |
|-------------|---|----|
| Figure 3.5 | One DOF model in contact with environment | 26 |
| Figure 3.6 | Simulation results of impedance control Position (Top Left), Contact Force (Top Right), Control Force (Bottom) | 27 |
| Figure 3.7 | Schematics for finger mechanism | 28 |
| Figure 3.8 | Description of finger X axis motion | 29 |
| Figure 3.9 | Description of finger Y axis motion | 29 |
| Figure 3.10 | Description of finger Z axis motion | 30 |
| Figure 3.11 | Description of finger Yaw axis motion | 30 |
| Figure 3.12 | Two closed loops in figure mechanism | 31 |
| Figure 3.13 | Schematics of scanner | 34 |
| Figure 3.14 | FEM model for scanner | 35 |
| Figure 3.15 | Deflection of frame depending on the position of sensor | 37 |
| Figure 3.16 | Deflection of sensor depending on the position of sensor | 38 |
| Figure 3.17 | First five mode shapes of frame | 38 |
| Figure 4.1 | Clustering Algorithm for error recovery | 41 |
| Figure 4.2 | Description of K Means Algorithm | 41 |
| Figure 4.3 | Description of Gaussian Mixture Model Algorithm | 43 |
| Figure 4.4 | Flow chart for error recovery | 45 |
| Figure 4.5 | Trajectory for position error recovery | 46 |
| Figure 4.7 | Trajectory for angular error recovery | 50 |
| Figure 4.8 | Variation in number of step for position error recovery ISO View (Left), Front View (Right) | 51 |
| Figure 5.1 | Specification of rotation stage, RTSS40 | 52 |
| Figure 5.2 | Experimental setup for angle measurement of scanner, Schematic of setup (Left) and Actual experimental setup (Right) | 53 |
| Figure 5.3 | Description for position accuracy and repeatability | 54 |
| Figure 5.4 | Histogram for measurement error | 56 |
| Figure 5.5 | Measurement and alignment of angular error with scanner and gripper | 57 |
| Figure 5.6 | Measurement of force data with given position error along XY trajectory | 58 |

| | | |
|-------------|---|----|
| Figure 5.7 | Actual position and velocity in XY trajectory depending on max velocity, 1mm/sec (Top), 2mm/sec (Middle), 5mm/sec (Bottom) ... | 59 |
| Figure 5.8 | Insertion force and moment when max velocity = 5mm/sec, Moment in x axis (Left), Moment in y axis(right) | 60 |
| Figure 5.9 | Clustering results with k means algorithm when max velocity = 5mm/sec, Moment in x axis (Left), Moment in y axis(right) | 61 |
| Figure 5.10 | Clustering results with k means algorithm on three datasets measured from same condition, Moment in x axis (Left), Moment in y axis(right) | 62 |
| Figure 5.11 | Clustering results with k means algorithm on three datasets measured from different velocity, 1mm/sec (Top), 2mm/sec (Middle), 5mm/sec(Bottom) | 63 |
| Figure 5.12 | Distribution of joint variables depending on covariance matrix | 65 |
| Figure 5.13 | Clustering results with gaussian mixture model algorithm on three datasets measured from same condition, Moment in x axis (Left), Moment in y axis(right) | 66 |
| Figure 5.14 | Clustering results with gaussian mixture model algorithm on three datasets measured from different velocity, 1mm/sec (Top), 2mm/sec (Middle), 5mm/sec(Bottom) | 68 |

Chapter 1

Introduction

1.1 Robotic Assembly and Peg-In-Hole Task

Since the advent of robot, it has been used in wide area of industries instead of human labors. However, the application filed of industrial robots is very limited to tasks like welding, pick and place and transporting which is simple and repetitive. Assembly task which requires combination of sensing and intelligence for mating parts is still challenging area to robots. Peg-In-Hole is one of the basic assembly tasks but it still takes a lot of time and is quite difficult to robot because of inaccuracy in sensing, difficulties in instantaneous event judgement required for mating parts. A lot of researches for aligning way of Peg-In-Hole task have been underway but it's still far behind successful results with respect to accuracy and error recovery time.

For successful robotic assembly, robust sensing and efficient recovery algorithm to detect the error is required for alignment between parts and damage prevention. Generally, conventional articulated manipulator has rigid structure for position accuracy thus small error can generate large reaction force between mating part which leads to damages on it. The stiffness of conventional articulated manipulator is around 500N/m, thus even small position error of 0.1mm can induce 50N force to the mating parts. In case of orientation misalignment, jamming and wedging shown in figure 1 can occur in which peg can't advance further. Jamming occurs when the insertion force vector of peg points too far off the axis of the hole [1]. Wedging occurs when the peg is trapped in the hole due to the compressive forces acting on the peg [1]. To avoid the jamming and wedging induced from orientation misalignment, compliance is suggested as a solution and device like RCC which uses compliance for passive aligning was researched and developed.

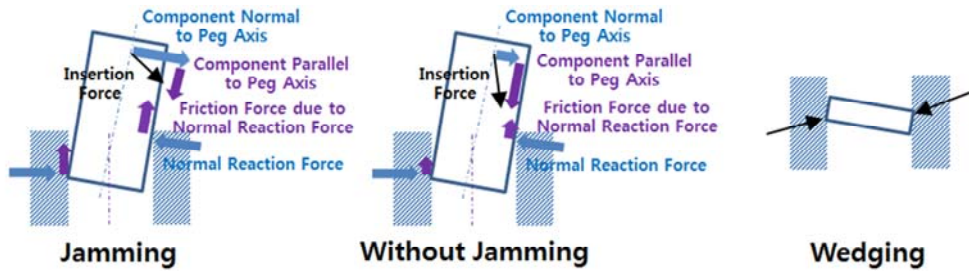


Figure 1.1 Conditions for Jamming and Wedging

1.2 Previous Research Works

A lot of researches for Peg-In-Hole task have been underway and aligning way between mating parts can be categorized into passive and active approaches as shown in figure 2. The passive approach [2-12] represented as RCC(Remote Center Compliance) uses the compliance and shape of mating parts for aligning mating parts, whereas the active approach [13-37] uses measurement information from vision, force or both of them. Passive approach [2-12] has strength in which aligning can be done passively without any other information and efforts but uses are limited because it depends on the characteristics of mating parts like chamfer size and length of peg. Active approach with force control [13-21] has strength maintaining the moderate force during insertion but the recovery time is unpredictable because the reaction moment used for error recovery depends on the various contact conditions which make it hard to distinguish the moment generation around the error position. Active approach with vision [22-28] is good for rough error estimation but accuracy is limited because of sensitivity in accuracy which depends on camera installed location and surrounding environment. Active approach with combination of force control and vision [29-37] utilize the both of information for better performance but the most of the cases the force and vision information are used independently for error recovery thus algorithms which fuse both of information efficiently need to be developed further.

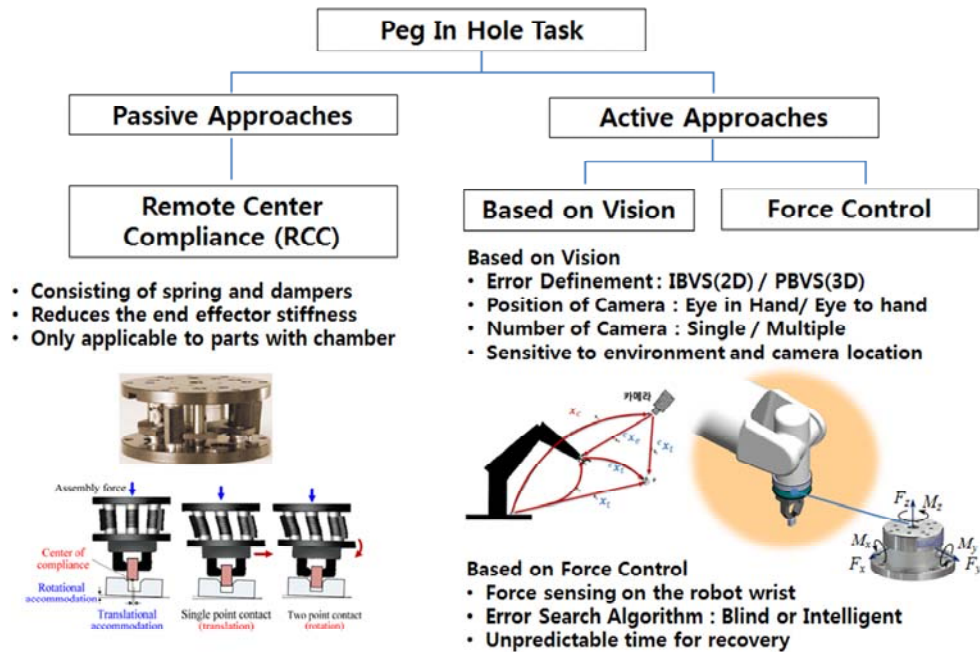


Figure 1.2 Classification of aligning way

1.2.1 Passive approaches

The RCC device which represents the passive approach was developed by Dr. Whitney at MIT and widely used with commercialized products. The RCC reduces the peg end point stiffness by using spring and dampers and use the induced motion from compliance for aligning when the force and moment are applied to the center of compliance usually set to the peg end by design. As shown in figure 1.3, single point contact and two point contacts occur in sequence during insertion and this induces the pure translational and rotational motion due to the generated force and moment at the peg tip, center of compliance. Although the RCC has the advantages in which it reduces scrap and damage by eliminating jamming and wedging and increase productivity, the practical use is limited depending on the chamfer size of mating parts and center of compliance determined by design.

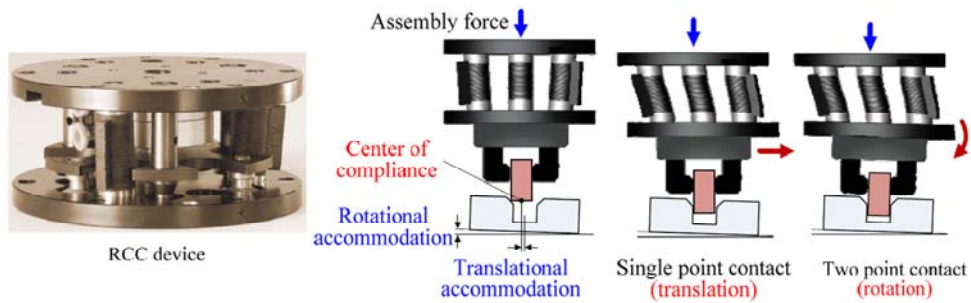


Figure 1.3 Principle of RCC from ATI Industrial Automation

To overcome the disadvantages on the fixed center of compliance, various design of VRCC (Variable Remote Center Compliance) is proposed by many researchers [5-7]. Zhao and Wu [5] constructed VRCC with electromagnetic driver and optical-electronic sensor and modulate the center of compliance by controlling the position of down plate with electromagnet. Lee et al. [6,7] proposed the VRCC mechanism constructed with elastomer shear pad by changing the stiffness of elastomer shear pad with the stiffness adjusting rod and rotation angle between plates holding elastomer shear pad. To utilize the deformation information, an effort to add sensor to RCC was also made. Bright and Deubler [8] made IRCC (Intelligent Remote Center compliance) with potentiometer array and make it possible to use deformation information during insertion. Although great effort have been made for RCC device, the disadvantages on limited application, only allowable restricted condition, still are not changed thus active approaches is inevitable for wide range of uses.

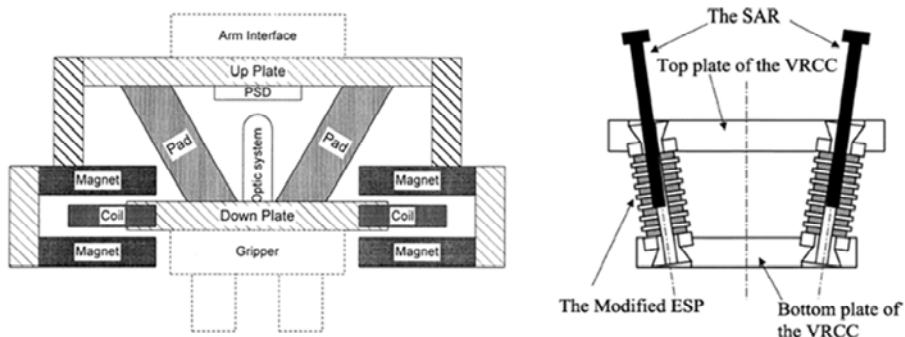


Figure 1.4 VRCC mechanism with electromagnet [5] (Left) and ESP modulation [7] (Right)

1.2.2 Active approaches

Active approach [13-21] based on force information usually use force information measured from the FT sensor mounted on robot wrist for maintaining moderate contact force between mating parts and estimating the position error. Depending on whether force information is used for error recovery, the search algorithm can be classified into blind and intelligent search. The blind search which does not use the force feedback information for error recovery usually use predefined trajectory like spiral trajectory covering search area. In contrast, the intelligent search uses the force feedback information with respect to robot position and estimates the position error with specific search way. Blind search has advantages that it's simple to use but the unpredictable recovery time depending on the position error is problem whereas intelligent search is good for finding the direction of error recovery but the absolute error measurement is impossible.

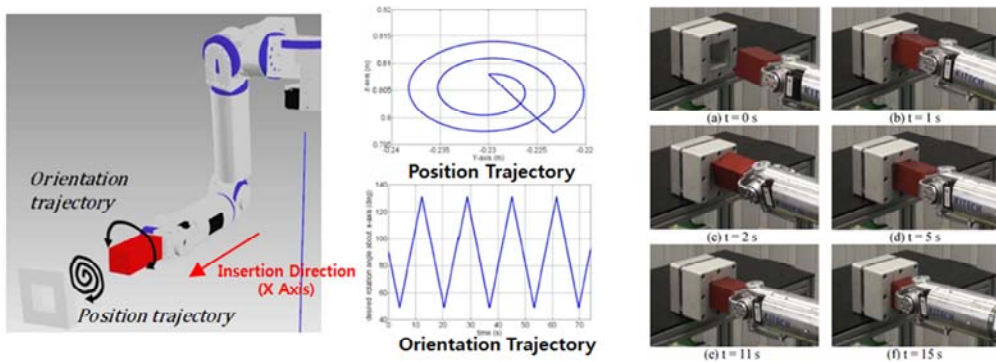


Figure 1.5 Blind search for square Peg-In-Hole [14]

Chhatpar and Branicky [13] investigated the efficient trajectory covering search area with given clearance for blind search and also presented tilt strategy, one of the intelligent search algorithms. Park et al [14] implemented hybrid force/position control and passive compliance control to the robot and utilized the spiral search trajectory for square Peg-In-Hole task. Imitating the way people insert the peg with force control, it achieved 100% success rate but unpredictable elapsed time before insertion is pointed out for problems to solve. Kim et al. [19, 20] proposed intelligent hole detection algorithms for square Peg-In-Hole by analyzing the force data which is

measured from different tilted posture over the hole. Although error in shape recognition and time for hole detection is less than 8% and around 10 seconds, it's hard to get direction of error recovery when the only angular error exists around the hole. Chen at al. [16] presented and tested the various search algorithm, spiral, probing and binary search for connector mating and compared each of search algorithms.

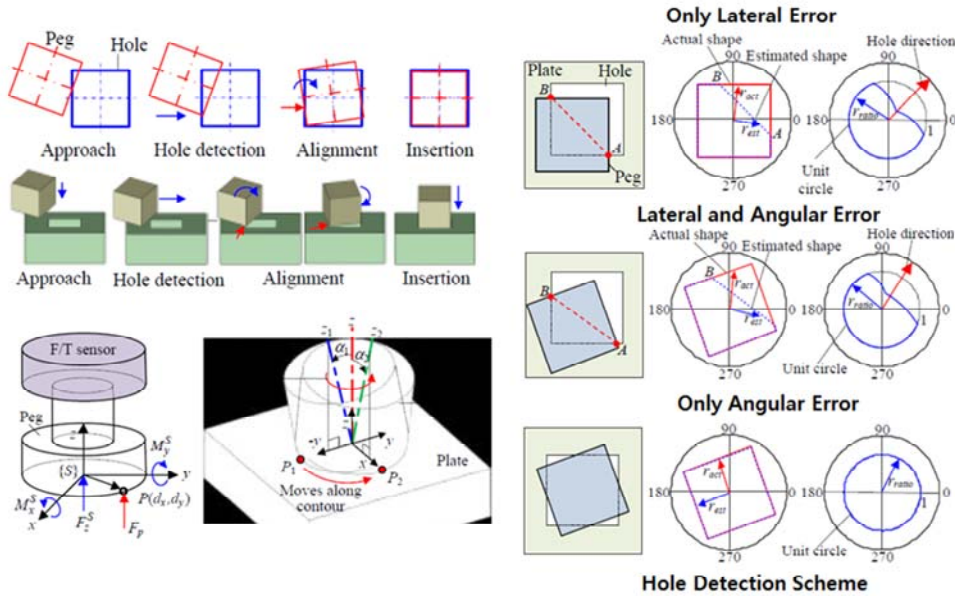


Figure 1.6 Intelligent search algorithm with shape recognition [19,20]

Researches on force and torque information for better position error estimation and fault detection during insertion also have been underway. The redundancy in generated force and torque corresponding to the different peg position makes it hard to estimate the position error because one-to-one matching is impossible. Dietrich at al. [17, 18] already pointed the problems on force-torque map originated from redundancy and proposed the way to generate force-torque map with minimum redundancy by combining the force-torque measurement taking from different tilted postures. The minimum union of redundancy map generated by combining the two different force-torque map reduces the redundancy but there still exists the considerable redundancy. The force pattern generated during insertion is also investigated for fault detection. Huang at el. [15] proposed the force model during connector insertion with four key phases and used fuzzy pattern for classifying four different fault cases, jammed insertion, connector lost, wrong connector and uncompleted insertion.

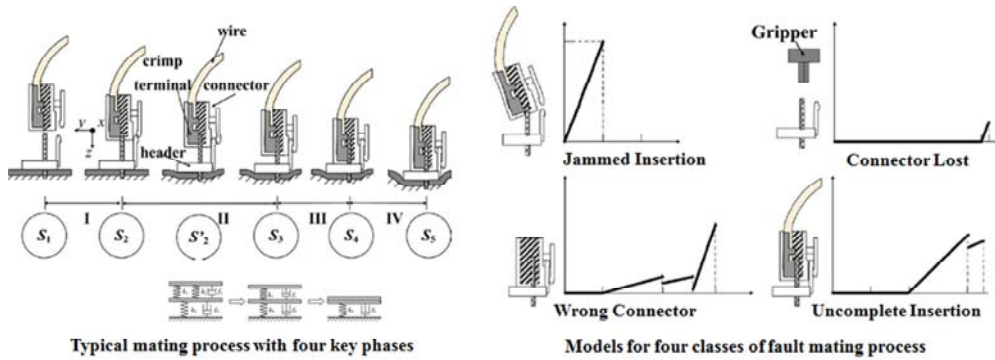


Figure 1.7 Fault detection model during connector insertion [15]

Active approach [22-28] based on vision information utilizes information from vision images for error recovery and can be classified as single or multiple cameras, eye in or to hand and IBVS(Image-Based Visual Servo) or PBVS(Position-Based Visual Servo) depending on the camera use condition, the number of camera used, position of camera installed and error definement method. Huang et al. [25] demonstrated fast Peg-In-Hole with two high speed camera configured as eye in hand and eye to hand and 3-DOF high speed active peg. The time for alignment was less than 1 second but the success rate was around 85% even though the tolerance between peg and hole was as large as 4mm. Chang and Lin [24] presented the Peg-In-Hole task in micro level around 100 μ m with three CCD cameras configured as eye to hand and two stages for peg manipulation. The visual-servo control for micro level assembly task was designed and tested but the success rate was around 80% and takes long time although it's installed and tested on well restricted environment. Jain et al. [27] designed and utilized compliant IPMC(Ionic Polymer Metal Composite) gripper and demonstrated the Peg-In-Hole tasks with two cameras configured as eye to hand. It demonstrated adding compliance at the tip with compliant gripper had advantages compared without compliance but the cameras location installed in bottom side plane of assembly for error estimation was not realistic for practical use. Wang and Cho [23] proposed to use image moments of feature for visual servoing to avoid image singularities and tested this method for aligning Peg-In-Hole in micro level. Fault diagnosis based on the

vision information was also researched by Di and Hwang [29]. The problems on fault diagnosis based on force data, only applicable to during insertion process was pointed out and fault detection algorithm based on vision after grasping was proposed for electric connector mating.

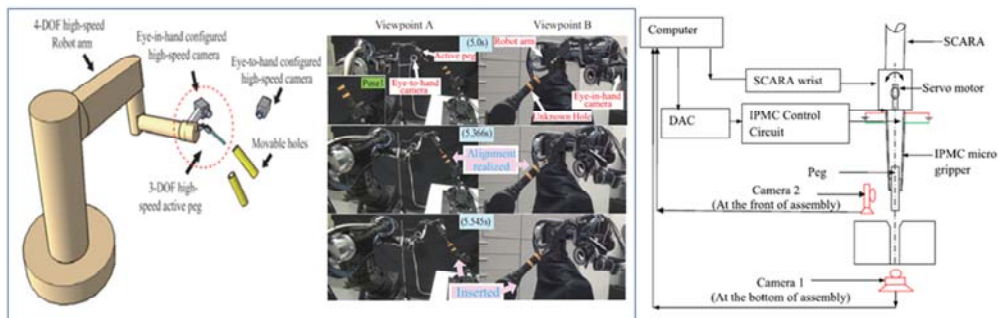


Figure 1.8 Peg-In-Hole based on vision with high speed camera [25] (Left) and IPMC gripper [24] (Right)

Researches utilizing the both of the advantages on force and vision have been also underway [29-36]. Robot Cell consisted of two articulated robot each of which equipped with 3D sensor and force sensor was developed and tested for electric connector mating by Haraguchi et al [33]. One robot equipped with 3D vision scanner pick up the cables in bulk state based on the vision information and the other robot performs the insertion task with spiral, probing and binary search based on the force information. The system for realistic problem on assembly was developed but the author pointed out remained problem on efficient error detecting. Feature detection and search algorithms of complexed shaped parts for assembly were also researched and proposed for high level of assembly task [30, 35, 36]. Imitating the way human assembly complex shaped parts, the feature was extracted first and sequence for aligning selected feature were made while maintaining appropriate insertion force with compliance control. It's demonstrated that the small position and orientation errors can be compensated effectively by using both of vision and force information.

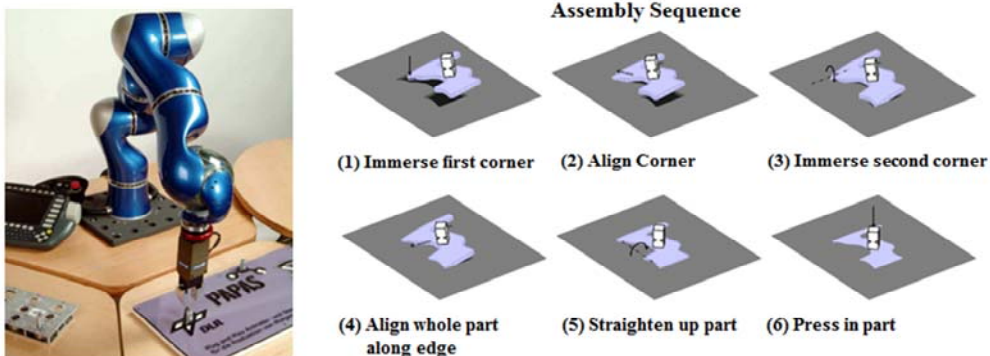


Figure 1.9 Complex shaped part assembly with force and vision information [30, 36]

1.3 Purpose and Contribution of Research

Despite of efforts which have been made for successful robotic assembly with passive and active alignment by many researchers, Peg-In-Hole task, one of the basic assembly tasks, which is easy to human is still challenging because instantaneous reaction to the events during insertion is impossible to robot. For successful Peg-In-Hole, the number of event occurring during insertion should be reduced through additional measurement information and robust algorithm for detecting error between mating parts needs to be developed.

A dexterous gripper with an angular error measurement system and reliable error estimation algorithm with clustering force dataset is proposed and tested for square Peg-In-Hole task in this dissertation. As stated above, the passive approaches using compliance can be applicable to limited use condition like chamfer size and the fact that the accuracy of vision depends on camera location and external environment requires the force feedback during insertion for damage prevention. However, additional measurement system which reduces the number of contact condition is necessary for the fast and robust error recovery based on force information. To make this goal, three main key features stated below are implemented in the system design and verified with experiments.

First of all, the dexterous gripper which consists of 4 DOF(Degree Of Freedom) two fingers embedded with 6 axis force sensors at the fingertip is designed for micro

manipulation of peg during error recovery. Following the way human uses fingers for manipulation of object and senses at the fingertip during assembly task, dexterous finger embedded with force sensors at the fingertip is designed and used for grasping and manipulating of peg. Large workspace of industrial robot constructed with serial structure is good for general tasks which do not require the interaction with environment but large effective mass and variation of it depending on postures has disadvantages in assembly task which requires interaction during recovery. The larger the mass to control, the more energy is consumed and shows slow response to applied force. Even more, a new controller design is required as mass changes. The utilization of dexterous gripper which has fast dynamic characteristics is required to overcome this.

Secondly, robust angle measurement system, scanner, consisted of 2DOF manipulator and laser distance sensor is also designed and implemented for measuring the angular error between peg and hole. As pointed out many researchers, the redundancy in force-torque map makes it hard to estimate error and this originates from the contact conditions between mating parts. Depending on the contact condition, the condition for reaction moment generation is decided thus angular error compensation is necessary for fast and reliable error recovery based on the reaction force. In case of square Peg-In-Hole, the contact condition can be classified into 5 cases depending on the number of edge and supporting area between peg and hole and reaction moment is generated in only one case. The fact that 3 cases originated from angular error distribute around target position validate the use of scanner, angular measurement system. With the angular error compensation, the number of contact condition can be diminished to 2 cases thus the recovery time can be shortened by decreasing the number of contact conditions.

Thirdly, clustering algorithm is applied to dataset constructed with the measured reaction moment and peg position data for extracting the position error between peg and hole. Even after angular error compensation, there exists another condition which generates no reaction moment in square Peg-In-Hole task, thus artificial intelligence which can extract the position error among dataset mixed with and without moment generation is required. Two representative clustering algorithms, K means algorithm

and Gaussian Mixture Model algorithm, is applied to the dataset and the accuracy and robustness of position error estimation in each of algorithms is also investigated. The K means algorithm which use non-model based approach assigns data into given number of cluster while minimizing sum of the squared distance between data and assigned cluster center. On the contrary, the Gaussian Mixture Model algorithm which use model based approach identifies the model parameter, mean and covariance, with expectation maximization and assigns the data into cluster with defined probability model. Both of algorithms are useful for assigning the each of data to the cluster with moment and no moment generation and the center position in each of cluster can be utilized for error estimation.

In summary, the proposed dexterous gripper makes it realized the use of finger for both of manipulation and sensing at the tip. Fast and reliable error recovery is also achieved by angular measurement system, scanner. Comparing with blind search which usually uses no information from sensors and long spiral trajectory for error recovery, the proposed measurement system and algorithms have advantages in terms of recovery time and no variation of it. Short XY trajectory which moves horizontally and vertically in given search area can be used and error recovery time have no variation regardless of position error by diminishing the number of contact conditions through angular error compensation. In case of blind search which use spiral trajectory, the number of position to check for position error recovery in given square search area is proportional to squared number of steps, N^2 , whereas that of XY trajectory is proportional to $4N$. The variation of recovery time in blind search is proportional to N^2 depending on the position error whereas XY search has no variation on it. The uncertainty in error estimation from redundancy in force-torque map, one of the main problems in error estimation, is solved with additional angle measurement and short trajectory uses.

Chapter 2

Contact Condition Analysis

2.1 Classification of Contact Condition

2.1.1 Connected Component Labeling

The redundancy in force-torque map is already pointed out and verified with the experiments by many researchers. But the contact condition, the main reason for this redundancy, has not been focused and investigated yet. To estimate the reaction force and moment acting on peg, the analysis model for contact condition corresponding to the position and angular error between peg and hole needs to be generated first. However, it's not an easy to make this analysis model because the contact condition changes severely with position and angular error and it also depends on the shape of peg and hole. For defining contact condition, the number of supporting region and number of edges crossing peg and hole needs to be found and general model which can be easily applicable to various shape of peg and hole needs to be developed.

Connected component labeling, one of the widely used algorithm in machine vision, is good candidates for defining contact condition described above. Connected component labeling is segmentation algorithm of binary images into partitions that corresponds to connected components as shown in figure 2.1. Depending on the used connectivity and labeling method, it's categorized into 4 or 8 connectivity and single or two or multi pass methods [37, 38]. The connected component is a set of all pixels in a binary image and connectivity of component depends on the applied connectivity method. Even if same binary image is used for connectivity component labeling, different results come out with different connectivity method as shown in figure 2.1. In case of 4 connectivity method, adjacent four point set defined in equation 2.1 is used and adjacent eight point set in equation 2.2 is used for 8 connectivity method.

$$A_4(x, y) = (x, y) + A_4 = \{(x + 1, y), (x - 1, y), (x, y + 1), (x, y - 1)\}$$

where, set $A_4 = \{(1,0), (-1,0), (0,1), (0,-1)\}$

(2.1)

$$A_8(x, y) = \{(x + 1, y + 1), (x + 1, y - 1), (x - 1, y + 1), (x - 1, y - 1), (x + 1, y), (x - 1, y), (x, y + 1), (x, y - 1)\}$$

where, set $A_8 = \{(1,1), (1,-1), (-1,1), (-1,-1), (1,0), (-1,0), (0,1), (0,-1)\}$

(2.2)

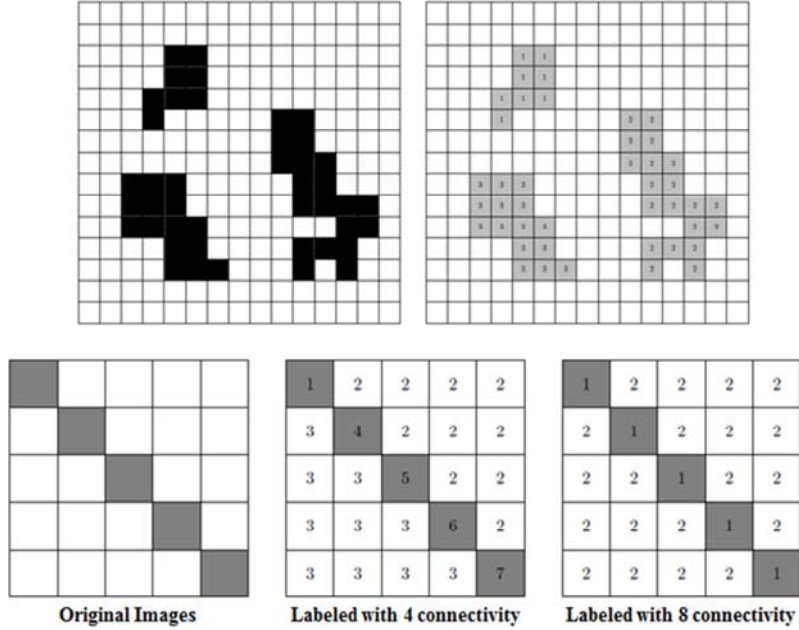


Figure 2.1 Example of connected component labeling (Top) and results with different connectivity (Bottom)

As described in following section, the binary images for every position and angular error is generated and used for connected component labeling.

2.1.2 Binary image generation procedures

To utilize the connected component labeling described above for finding contact condition, the binary image generation procedures shown in figure 2.2 is used and the images for given position and angular error in planar contact condition is made for analysis. First of all, the peg is allocated with N by N node with predefined small step size and the each node position of peg with each of given position and angular error is calculated in terms of hole coordinate as described in equation 2.3.

$$\begin{aligned}
P_{x' \text{ in hole coordinate}} &= P_x \cos\theta - P_y \sin\theta + dx \\
P_{y' \text{ in hole coordinate}} &= P_x \sin\theta + P_y \cos\theta + dy
\end{aligned}$$

where, P_x is the node position of peg in x axis
 P_y is the node position of peg in y axis
 dx is the position error in x axis
 dy is the position error in y axis
 θ is the angular error

(2.3)

Then, the position of each node is checked whether it's inside the hole or not and marked with 1 or 0 depending on this node condition. Finally, the binary image indicating the status of contact conditions between peg and hole is generated and used for connected component labeling.

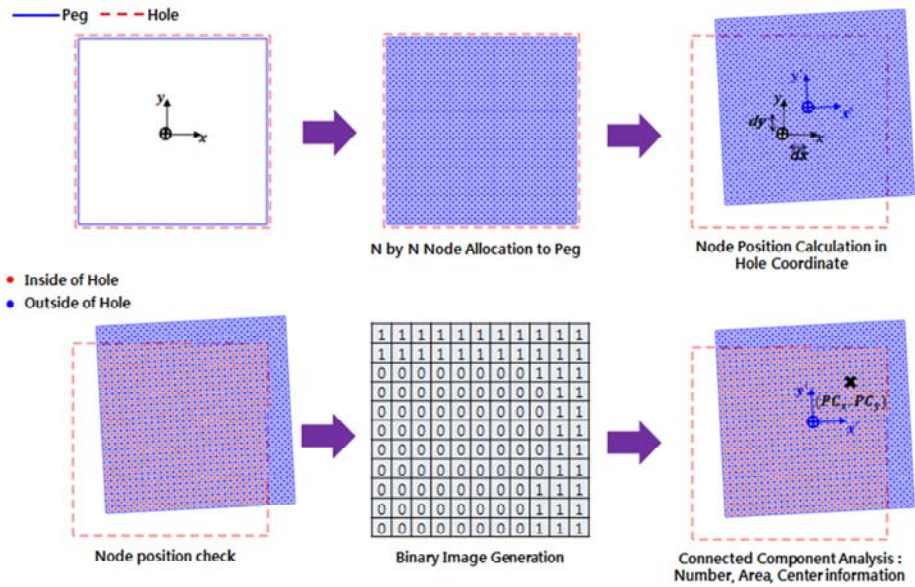


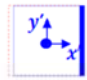





Figure 2.2 Binary image generation procedures for Connected Component labeling

2.1.3 Analysis results for contact condition

The contact condition can be defined with the number of connected component and edge crossing between peg and hole. In case of circular Peg-In-Hole in which only position alignment is important, there is only one case with one connected component and one edge and there is no redundancy in force-torque map. However, there are five

cases in square Peg-In-Hole in which both of the position and angular alignment is important and moments are generated in only one case. The axis of moment indicated in figure 2.3 is always located outside of peg center position in four cases thus no moment is generated because the insertion force acting on peg center is always inside of axis of moment. Therefore, the redundancy in force-torque map already pointed by many researchers arises and this makes it hard to use the force feedback information for error estimation.

To estimate the direction and magnitude of errors, the one to one matching between position and force feedback information is desirable but the fact that no moment is generated in most of contact cases requires for diminishing the number of cases in contact conditions and efficient search algorithms. The five contact conditions in square Peg-In-Hole can be categorized by the error source, position or angular error and moment generations shown in figure 2.3. Two cases arise by position error whereas the other three cases mainly arise by angular error. To reduce the uncertainty originated from contact condition, the angular error compensation is more effective than position error compensation by removing three cases.

| | Position Error | Angular Error | Position + Angular Error |
|-----------|---|---|--|
| Moment |  <p>Case 1 No of CC : 1 No of Edge : 1</p> | | |
| No Moment |  <p>Case 2 No of CC : 1 No of Edge : 2</p> |  <p>Case 5 No of CC : 4 No of Edge : 4</p> |  <p>Case 3 No of CC : 2 No of Edge : 2</p>  <p>Case 4 No of CC : 3 No of Edge : 3</p>  <p>Case 5 No of CC : 4 No of Edge : 4</p> |

* No of CC : Number of Connected Component
* No of Edge : Number of edge crossing the peg and hole

Figure 2.3 Five contact conditions in square Peg-In-Hole

The figure 2.4 and table 2.1 indicates the simulation results for distribution of the five contact conditions and numbers of each case conducted on the square peg and hole with the size of 30mm and 30.2mm. The simulation is executed in small ranges of position and angular error, $-3\text{mm} < dx, dy < 3\text{mm}$ and $-3^\circ < \theta < 3^\circ$ with small step size 0.1mm for position error and 0.1 degree for angular error.

Concerning to the cases which does not generate moment, the three cases, 3, 4 and 5 originate from angular error is distributed around the origin position of hole whereas the case 2 widely spreads out the simulated range. Even more, it's clearly observed that the size of distribution area for the case 3, 4 and 5 increases with the increased angular error leading to bigger uncertainty around origin position of hole. The number of case 1 which is useful by providing the moment information does not change with the decreased angular error range whereas the number of three cases, 3, 4, and 5 decreases significantly with it. Therefore, it's most effective to compensate the angular error with angle measurement for error estimation based on force information.

However, the efficient algorithm with short search trajectory is still required for error estimation even after the angular error compensation. Even after angular error compensation, there still exists case 2 which is widely spread all around the origin position of hole and takes most of search area. In contrast to that, the case 1 only distributed along restricted condition when only one of peg position does not align with the hole position. Considering this, it's necessary to generate efficient search trajectory and error estimation algorithm to pick up the case 1 among case 2 which is widely spreads out on search area.

Table 2.1 Number of contact conditions in each case depending on the angular error

| No of Event | $-3^{\circ} < \theta < 3^{\circ}$ | $-1^{\circ} < \theta < 1^{\circ}$ | $-0.1^{\circ} < \theta < 0.1^{\circ}$ |
|-------------|-----------------------------------|-----------------------------------|---------------------------------------|
| Case 1 | 360 | 360 | 360 |
| Case 2 | 176192 | 71312 | 10800 |
| Case 3 | 44664 | 6168 | 0 |
| Case 4 | 1672 | 168 | 0 |
| Case 5 | 4090 | 130 | 0 |
| Total | 226978 | 78138 | 11160 |

Distribution of contact condition for five cases

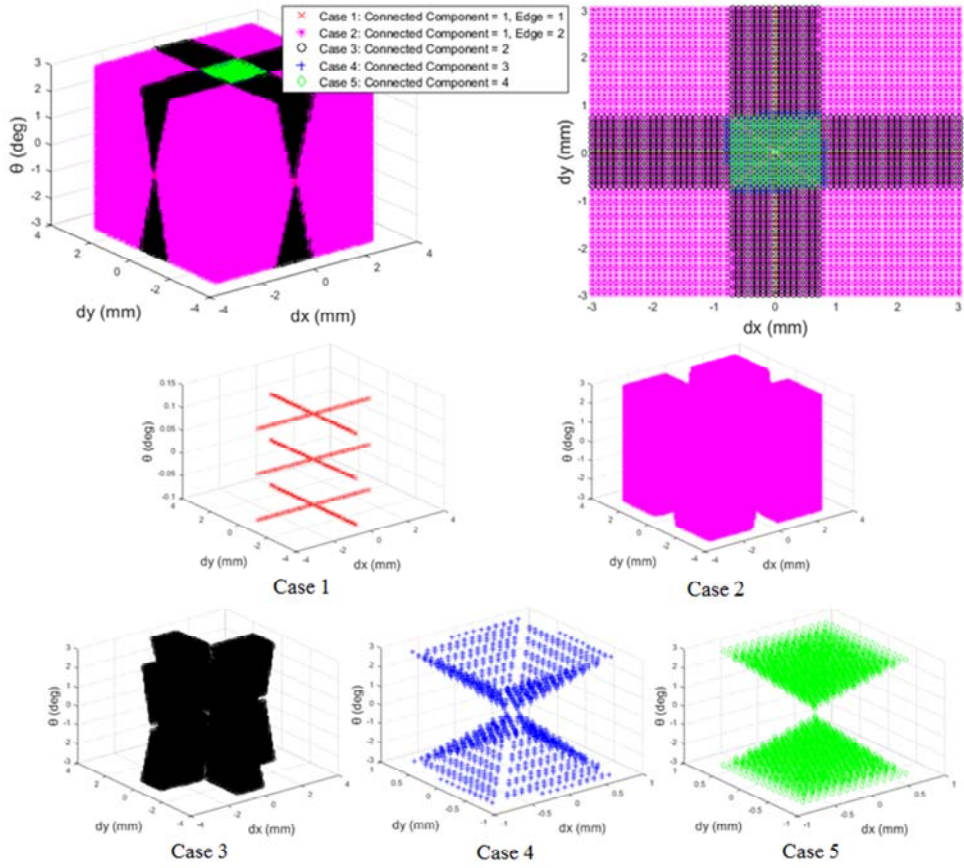


Figure 2.4 Distribution of five contact conditions in square Peg-In-Hole

2.2 Force and Moment depending on contact condition

The moment generation in x and y axis occurs only in case 1 where the one of peg position is aligned to origin position of hole with no angular error. In other words, the moment about x axis is generated when there is almost no position error in x axis and the moment about y axis is generated in the same way as in figure 2.5. It can be clearly observed that only small number of event represented with line for moment generation exist among most of events represented with square area for non-moment generation. Although this aspect requires to search around hole origin position, this restricted constraint for moment generation is also good for error estimation.

Moment in X and Y Axis with respect to Contact Condition

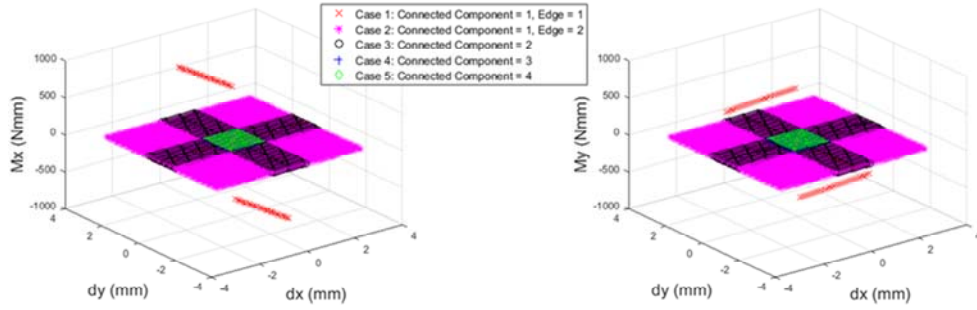


Figure 2.5 Moment generation with respect to contact condition

To estimate the reaction force and moment at the finger, the center position among the contact area the insertion force acting on is necessary to find. The center position of each connected component in pixel is calculated and transformed into the actual position in peg coordinate to use for the finger reaction force estimation. The figure 2.6 below indicates the center position of each connected component from connected component labeling for representative four cases.

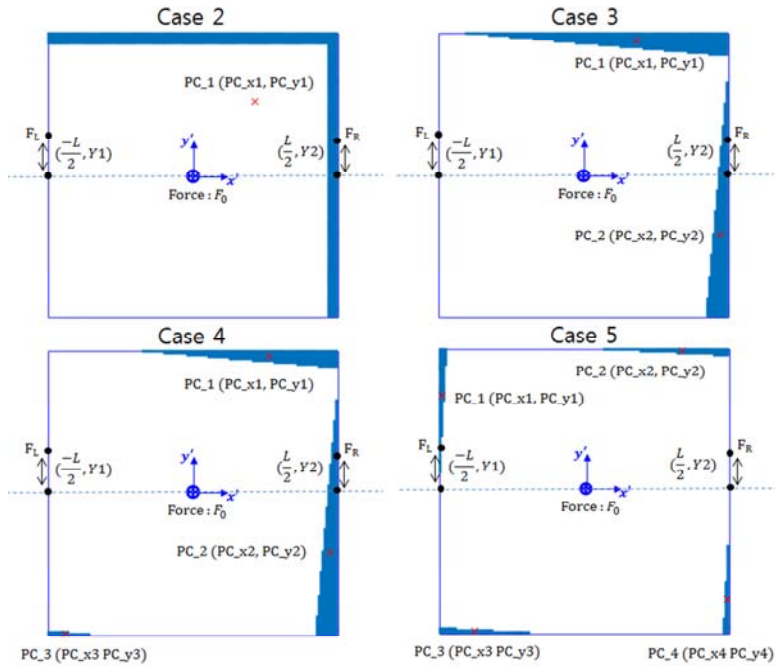


Figure 2.6 Center position estimation from Connected Component Labeling

Following the notation on figure 2.7, the reaction force acting on peg is calculated first and the force and moment at each finger is calculated based on that. In static equilibrium condition, the reaction force and moment acting on the peg is,

$$\begin{aligned}\sum F &= F_0 + \sum_{i=1}^n F_i = 0 \\ \sum M_{y0} &= \sum_{i=1}^n -F_i PC_{xi} \\ \sum M_{x0} &= \sum_{i=1}^n F_i PC_{yi}\end{aligned}\tag{2.4}$$

Where, n is the number of contact conditions

Based on the reaction force and moment found above, the reaction force at each finger can be calculated as follows.

$$\begin{aligned}\sum F &= F_0 + F_L + F_R = 0 \\ \sum M_y &= M_{y0} + F_L \frac{L}{2} - F_R \frac{L}{2} = 0 \\ \sum M_x &= M_{x0} + M_L + M_R = 0\end{aligned}\tag{2.5}$$

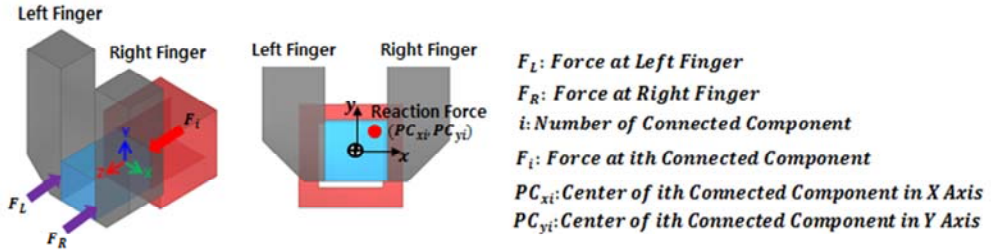


Figure 2.7 Reaction force and moment at the finger

However, the moment is generated depending on the contact condition as stated above. Therefore, the force and moment at the finger in case 1 is changed with the center position of connected component whereas that of the other cases has same values which makes it hard to distinguish the error estimation. The reaction force and moment at peg and fingertip is summarized on table 2.2.

Table 2.2 Summary of reaction force determined from contact condition

| | Contact Condition between peg and hole | |
|---|--|--|
| | Case 1 | Case 2, 3, 4, 5 |
| Moment | Generated | Not Generated |
| Reaction Force between Peg and hole | $\sum F = \sum F_i = -F_0$ $\sum M_{y0} = \sum -F_i PC_{xi}$ $\sum M_{x0} = \sum F_i PC_{yi}$ | $\sum F = \sum F_i = -F_0$ $\sum M_{y0} = \sum -F_i PC_{xi} = 0$ $\sum M_{x0} = \sum F_i PC_{yi} = 0$ |
| Force at the Finger | $\sum F = F_0 + F_L + F_R = 0$ $\sum M_y = M_{y0} + F_L \frac{L}{2} - F_R \frac{L}{2} = 0$ $\sum M_x = M_{x0} + M_L + M_R = 0$ | $\sum F = F_0 + F_L + F_R = 0$ $\sum M_y = F_L \frac{L}{2} - F_R \frac{L}{2} = 0$ $\sum M_x = M_L + M_R = 0$ |

Chapter 3

Design Synthesis of Gripper and Scanner

3.1 Overall Design Overview

The proposed design and specification of gripper and scanner, angular measurement, system is described in figure 3.1. The overall size and weight of the entire system is 300 x 240 x 215mm and around 4kg. To give degree of freedom to finger and scanners, ten small linear step motors constructed with combination of three main components, step motor, ball screw and the incremental encoder with the resolution of 16,000 pulses per revolution are embedded in the design. The lead of ball screw in linear step motors is selected as 0.635mm to give precise accuracy in position control and two types of linear step motors are used.

Ten motor drivers from Fastech as shown in figure 3.2 are also connected to the each of motor and controlled with EtherCAT protocol. Two mode of operations, Cyclic Synchronous Position mode and Profile Position mode in EtherCAT protocol are used for position controller design of finger and scanner. In case of finger, the CSP mode is used for controller design to give synchronous movement of two fingers for peg manipulation whereas PP mode is used for controller design of scanner.

The dexterous gripper which not only can grasp but also manipulate the object for error recovery is consisted of two symmetric fingers each of which has 4 DOF with small stroke, 30mm, $\pm 5\text{mm}$ and $\pm 5\text{deg}$, in X, Y, Z and Yaw axis respectively for micro manipulation of peg and 6 axis force sensors which has resolution 150mN and 2.5mN in force and moment measurement are embedded at the fingertip. The mass of each finger is around 1.5kg and it's operated by parallel mechanism with combination of link and joint. The light weight and no variation of effective mass in finger which determines the dynamics characteristics has advantages on the small peg manipulation compared with using the commercial industrial robots in assembly task which require the interaction with environment during insertion.

The scanner, angular measurement system, consists of 2 DOF manipulator which has stroke 50mm and 35mm in X and Z axis respectively and the laser distance sensor with the resolution of $0.01\mu\text{m}$ mounted at the end of manipulator. The total weight of scanner is around 1kg. Instead of using vision which is sensitive to environment and requires for right camera location for accuracy, the laser distance sensor is selected to use for angle measurement. The height along the top plane of peg and hole is measured and this height is transformed to angle by applying trigonometric function with the distance the manipulator moved along the surface of peg and hole.

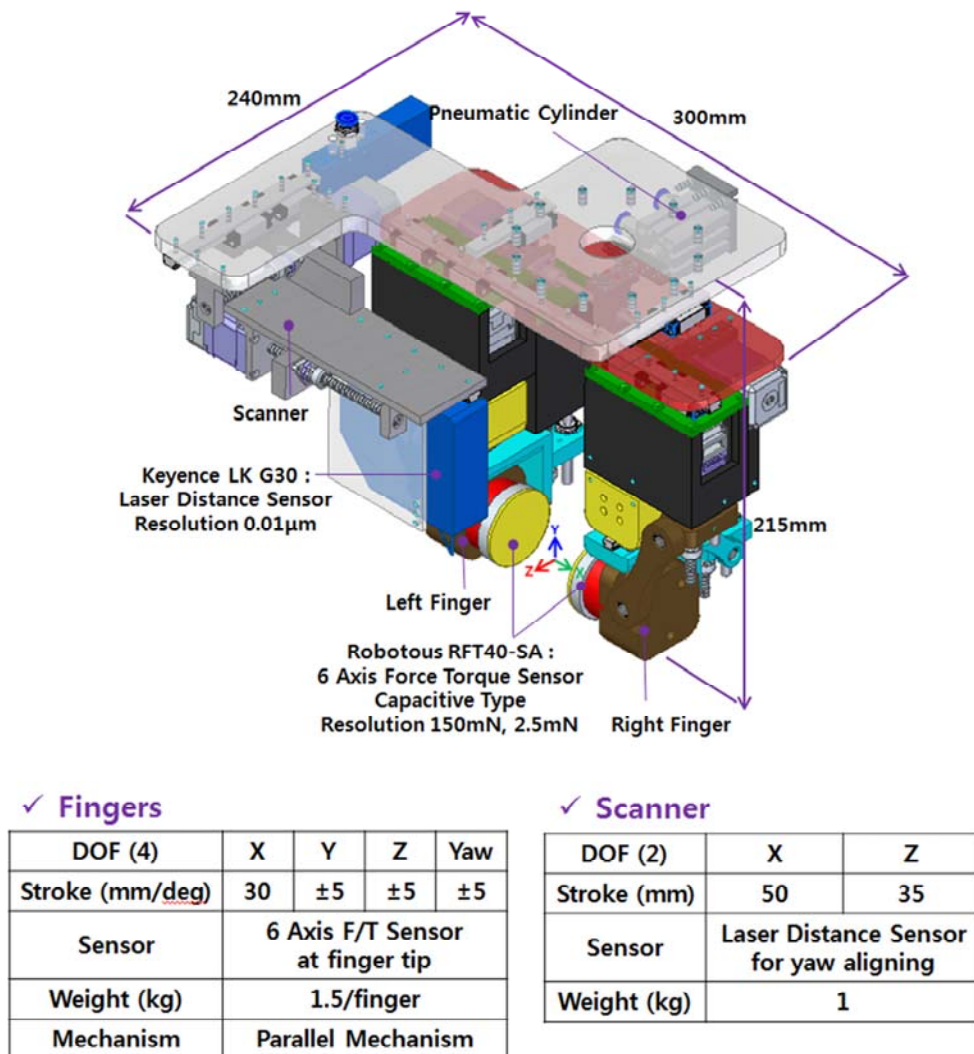


Figure 3.1 Schematics and specification of finger and scanner

CompactRIO 9082, general controller and data acquisition system from National Instrument is used for controlling ten motors and getting signals from force and laser

distance sensor. The prototype and schematics of electronics hardware for entire system is indicated in figure 3.2. The CRIO 9082 controls and communicates with the ten motor drivers from FASTECH through EtherCAT communication protocol. The signal from force and distance sensor is acquired with RS485, serial communication, and Analogue to Digital Converter respectively. All the information, actual position of each motors, force and distance information is transmitted to host PC with TCP/IP communication and recorded into the file with the period of 10ms for estimation of position error.

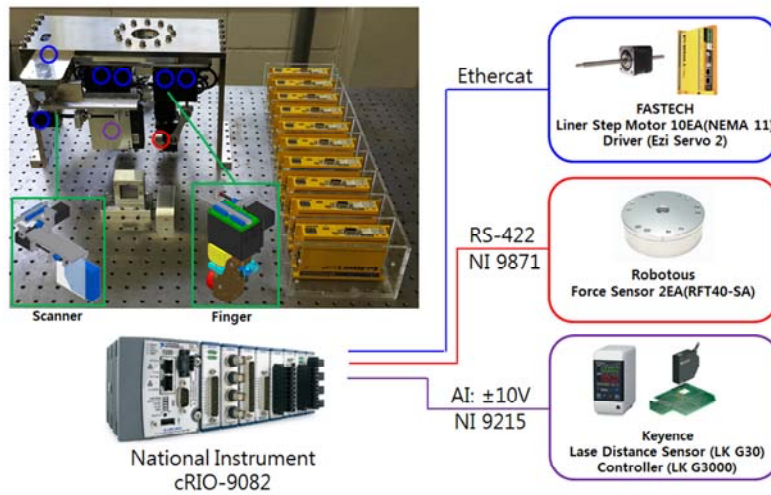


Figure 3.2 Prototype and schematics of electronics hardware

3.2 Design and Mechanism of Finger

3.2.1 Advantages of parallel mechanism

The each finger is constructed with parallel mechanism and actuated with four small linear step motor mounted on the base of the frame. Generally, structure operated with parallel mechanism has advantages on fast dynamic characteristics and no variation of it compared with structure with serial mechanism. Most of industrial articulated robots are constructed with serial structure in which reducer and motor is located at each joint. Therefore, the effective mass at the end effector is always larger than payload itself and it also varies with the manipulator posture severely. The mass matrix in joint space which describes the inertial mass acting on joint can be calculated with summing up two kinetic energy terms originated from position and rotation velocity changes in

given position and orientation. Using both of Jacobins describing the linear and angular velocity and inertial terms defined in each end effector position, mass matrix in each joint can be calculated as follows.

$$M = \sum m_i J_{vi}^T J_{vi} + J_{wi}^T I_i J_{wi}$$

where, J_{vi} = Linear velocity of ith link
 J_{wi} = Angular velocity of ith link
 m_i = Mass of ith link
 I_i = Inertia tensor of ith link

(3.1)

The mass matrix in joint space can be converted to the effective mass in cartesian space which describes the inertial mass for object manipulation in cartesian coordinate as follows.

$$A = J^{-T} M J^{-1}$$

where, J = Jacobian from manipulator kinematic model

(3.2)

Taking the commercial UR10, serially structured light weight arm from Universal Robot, as an example, the effective mass corresponding to end effector position within the workspace is calculated and variation of that along end effector position is analyzed. As shown in figure 3.3, UR 10 follows the serial structure of articulate industrial robot and is constructed with three actuators and two links to locate the end effector in 3 dimensional space. In principle, the inertial mass acting on the each joint is determined by the distributed mass from end effector to joint. Although two actuators located on the base does not affect on the inertial mass acting on joint, the payload and third actuator located at the end of each link makes the inertial mass changed with end effector position. Reflecting the specification of design and mass properties of UR 10 described in figure 3.3, the calculated effective mass in each axis, X, Y and Z axis, in given position is shown in figure 3.4.

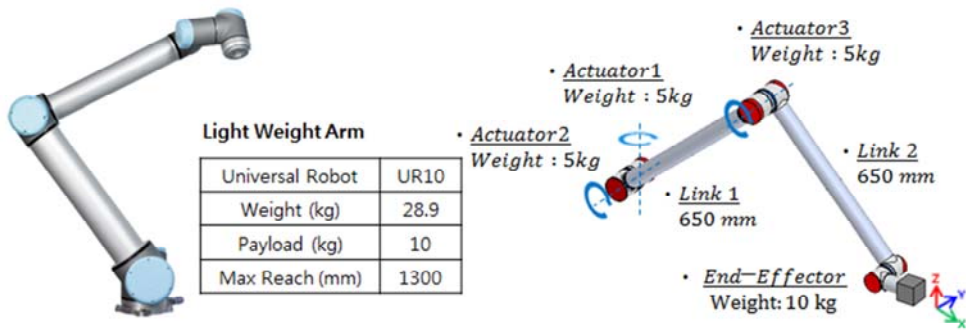


Figure 3.3 Articulated robot arm with serial structure

Excluding the position around singular position, full stretched out or folded posture, the effective mass acting on each axis varies from 10kg to 180kg along the end effector position. The effective mass is always larger than the payload itself the robot need to manipulate due to the changes on inertial mass acting joint originated from distributed mass in robot structure. It's clearly seen that the effective mass on each axis increases when the end effector is positioned far away from the origin. The effective mass is the one of the main parameters which determines the dynamic characteristics of system. This increased effective mass and variation of it within workrange of robot generates the inefficiency problems in force controller design which is necessary for maintaining stable contact at the end effector in assembly task.

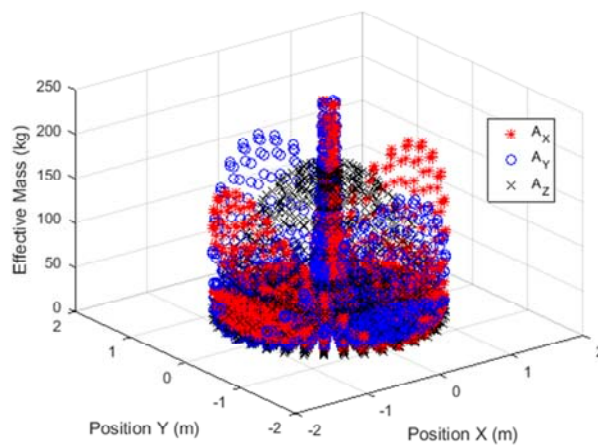


Figure 3.4 Effective mass depending on the position of end effector

The inefficiency in force controller design for serially structured robot can be demonstrated with the simple interaction model with environment indicated in figure 3.5. The increased and variation of effective mass not only causes to make new force controller design for given position but also needs to input additional control force to satisfy the constraint like settling time, overshoot and desired contact force.

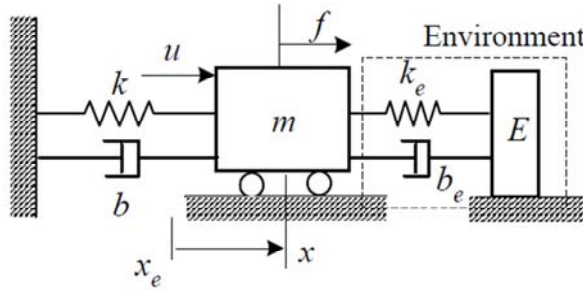


Figure 3.5 One DOF model in contact with environment

Considering the second order system in figure 3.5, the dynamic equation of motion for the system which interacts with environment is,

$$m\ddot{x} + b\dot{x} + kx = f + u \quad (3.3)$$

The external force from environment, f , and control force, u , with desired impedance for satisfying the constraint in force control is defined as,

$$f = -b_e\dot{x} - k_e(x - x_e)$$

$$\text{where, } x_e = \text{Equilibrium position} \quad (3.4)$$

$b_e, k_e = \text{Damping coefficient and stiffness of environment}$

$$u = (m - m_d)\ddot{x} + (b - b_d)\dot{x} + (k - k_d)x + b_d\dot{x}_d + k_d x_d$$

$$\text{where, } m_d, b_d, k_d = \text{Desired impedance, mass, damping coefficient and stiffness} \quad (3.5)$$

$$\dot{x}_d, x_d = \text{Desired velocity and position}$$

Plugging in the Eq 3.4 and 3.5 to Eq 3.3 gives modified dynamics of system with desired impedance as follows.

$$m_d\ddot{x} + b_d(\dot{x} - \dot{x}_d) + k_d(x + x_d) = b_d\dot{x}_d + k_d x_d + k_e x_e \quad (3.6)$$

The parameters stated in below are plugged into the model above and simulation is executed with two different desired mass, 10kg and 1kg, to check the influence of actual effective mass on response of system. The figure 3.6 indicates the position, contact force and control force in impedance control. The actual mass of the system is set to 10kg as indicated below, thus no control force is necessary to change the dynamic characteristics of system when desired mass is 10kg. However, bigger mass causes slow responses which lead to long settling time. In contrast to that, the fast response is achieved with additional control force when the desired mass is set to 1kg. Although changing the dynamic characteristics of system to satisfy the constraint is possible with controller design, it's verified that the bigger energy is required as the difference between desired and actual mass gets larger. In this point, the serially structured robot has intrinsic weakness with bigger effective mass which requires for the additional effort for control in interacting with environment.

$$m = 10\text{kg}, b = 20\text{Nsec/m}, k = 1000\text{N/m}, b_d = 20\text{Nsec/m}, k_d = 1000\text{N/m}$$

$$b_e = 0, k_e = 500000\text{N/m}, x_e = 0.01\text{m}, \dot{x}_d = 0, x_d = 0.02\text{m}$$

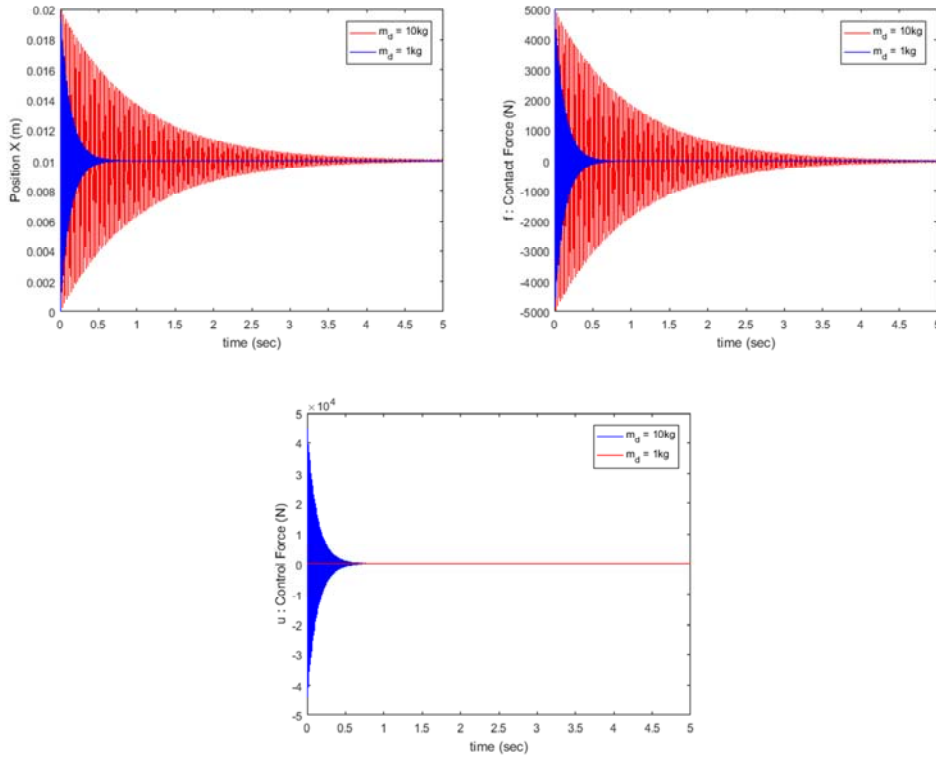


Figure 3.6 Simulation results of impedance control
Position (Top Left), Contact Force (Top Right), Control Force (Bottom)

3.2.2 Mechanism description of finger

The parallel robot in which the most of actuator are located in the base has superior dynamic characteristic, low mass and no variation, to serial robot. To make use this advantage of parallel mechanism, three axes, Y, Z and Yaw axis is actuated by three linear step motors mounted on the base in parallel as indicated in figure 3.7 and combination of links, rotation and ball joint is used to change the direction of linear step motor movement. In case of Y axis movement, the motion is made by synchronized movement of three axes whereas the motion in Z and Yaw axis is made by link connected to motor mounted on the base through rotational and ball joint respectively. All of the three axes, Y, Z and Yaw axis, are attached to the end of X axis serially which is used for grasping object. Two types of linear step motors, captive or external type, are used as shown in figure 3.7 with same lead size of ball screw, 0.635mm. The captive type is embedded for Y axis whereas external type is used for other three, X, Z and Yaw, axis.

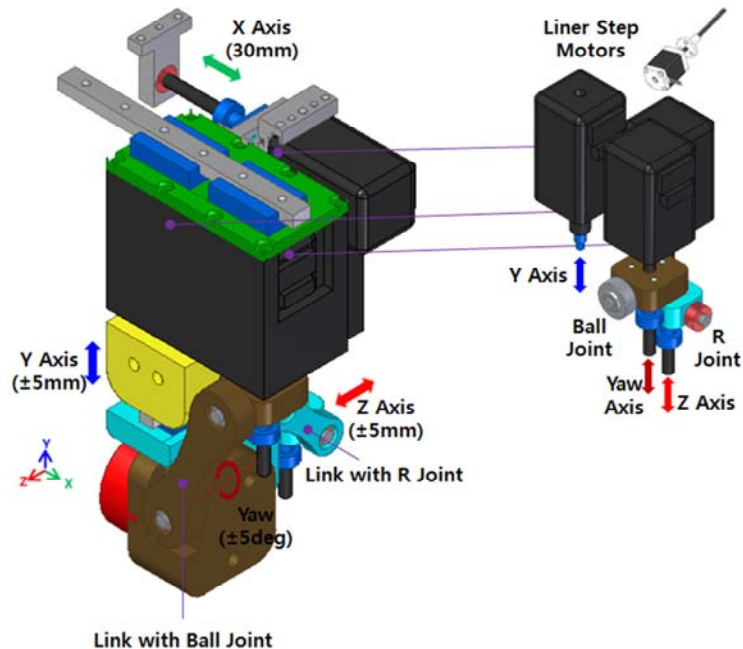


Figure 3.7 Schematics for finger mechanism

The working principle of finger mechanism in each axis stated above is well described with the motor, link, joint location and working range from figure 3.8 to figure 3.11

with following the coordinates indicated in figure 3.7.

Finger X Axis Motion

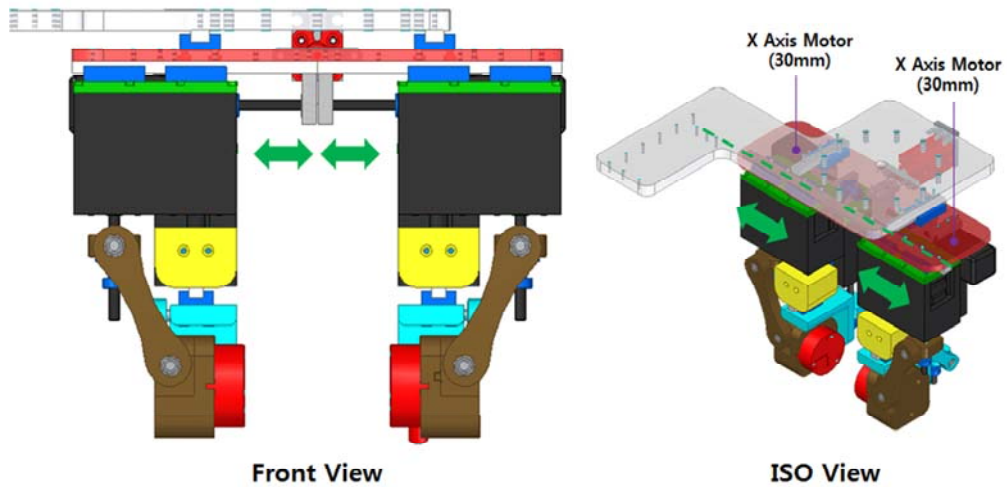


Figure 3.8 Description of finger X axis motion

Finger Y Axis Motion

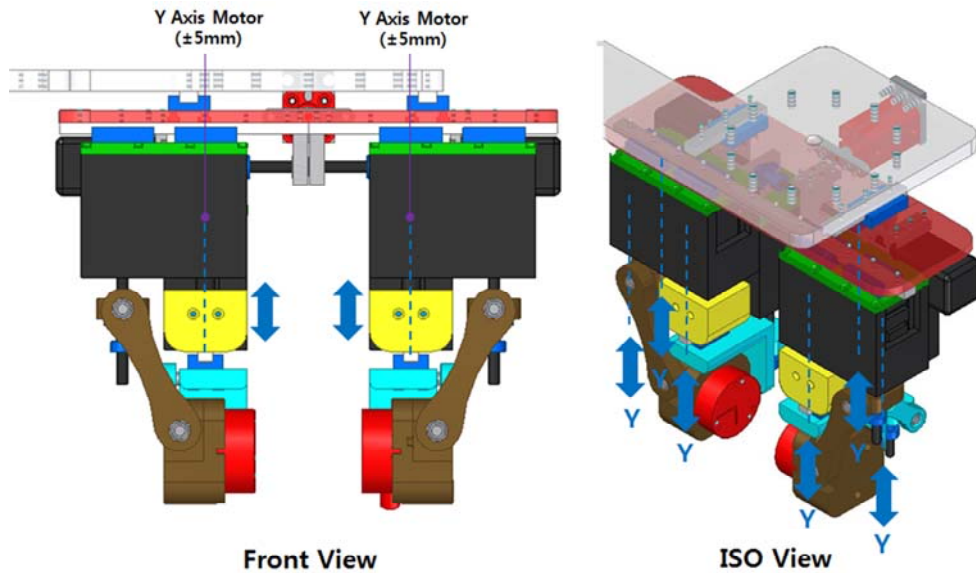


Figure 3.9 Description of finger Y axis motion

Finger Z Axis Motion

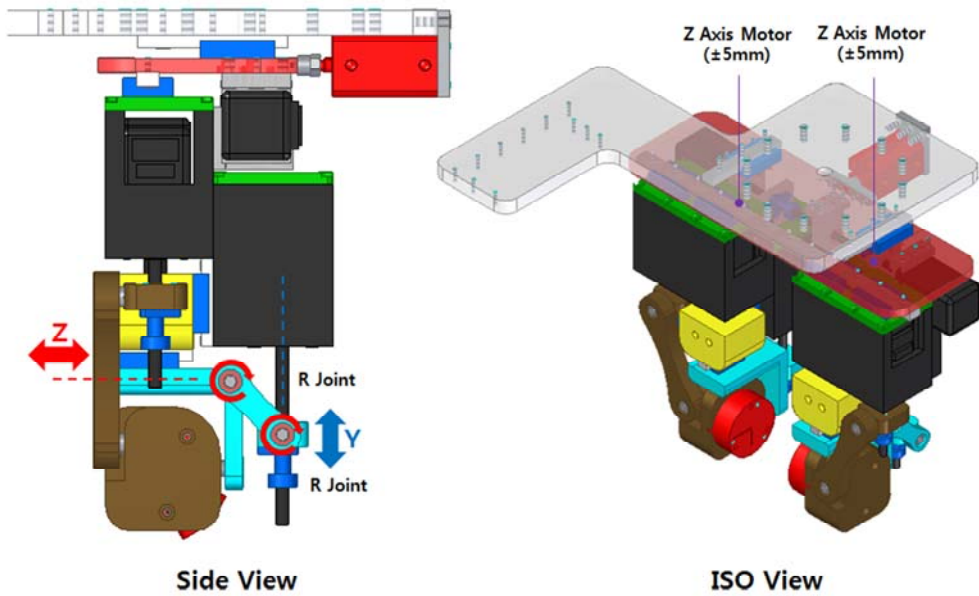


Figure 3.10 Description of finger Z axis motion

Finger Yaw Axis Motion

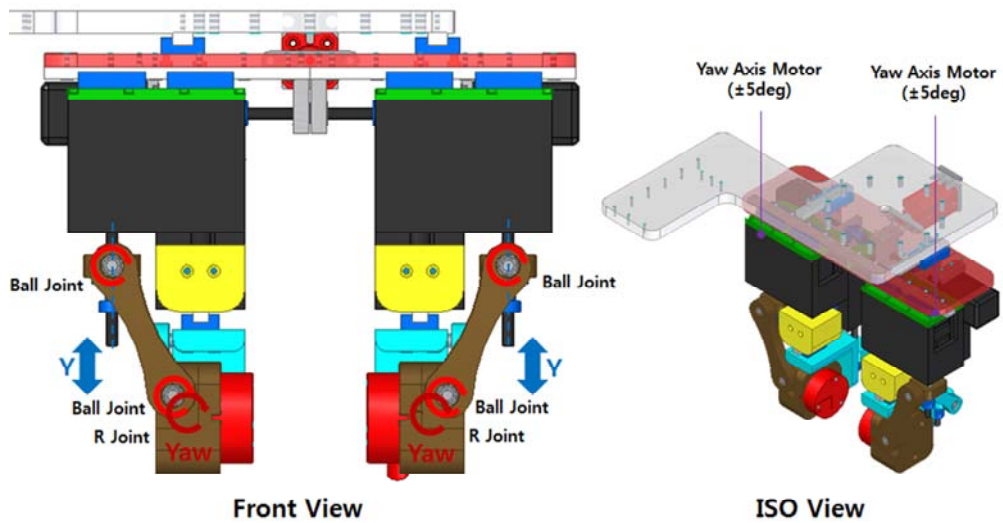


Figure 3.11 Description of finger Yaw axis motion

3.2.3 Kinematic of finger

The finger constructed with parallel mechanism has two closed loop in structure as shown in figure 3.12 and the motion in Z and Yaw axis should be synchronized to the motion from other axes as described in Eq 3.7. The order of actuation in finger structure is Y, Z and Yaw axis, thus the compensation for movement from upper level is inevitable for precise position control. The stroke in Z and Yaw axis is determined by the angle between the drive link and horizontal axis and the inverse kinematics describing this angle with respect to the linear stroke in Z and Yaw motor axis is necessary for finger manipulation.

$$\begin{aligned}
 X &= Stroke_x \\
 Y &= Stroke_y \\
 Z &= Stroke_y + L_z \theta_z \\
 Yaw &= Stroke_y + L_{\theta z} \theta_{\theta}
 \end{aligned} \tag{3.7}$$

where, $Stroke_i$ is the stroke made by i axis

L_z and θ_z is the length and angle of link in Z axis

$L_{\theta z}$ and θ_{θ} is the length and angle of link in Yaw axis

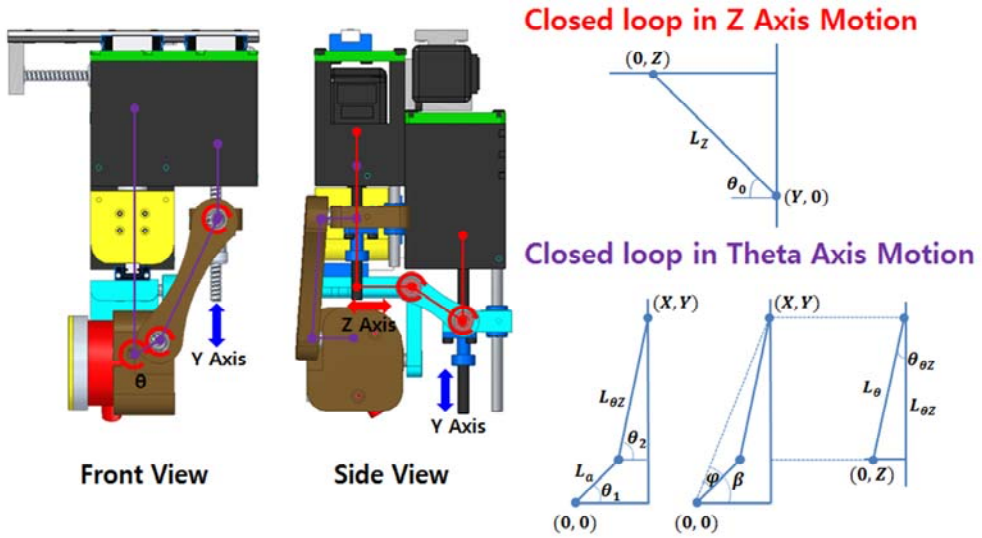


Figure 3.12 Two closed loops in figure mechanism

In case of Z axis, it's actuated by link connected to the motor with rotational joint right below the Y frame. Following the notation in figure 3.8, the relation between angle and linear stroke of motor in Z axis which moves in parallel with Y axis can be described as follows. Let the Y_0, Z_0 and θ_0 is the position and angle at origin, the position in Z Axis, Z, determines the angle of link with respect to horizontal line as indicated in Eq 3.9.

$$\begin{aligned} Y_0 &= L_Z \sin \theta_0 \\ Z_0 &= L_Z \cos \theta_0 \end{aligned} \quad (3.8)$$

$$\begin{aligned} Z_0 + Z &= L_Z \cos(\theta_0 + \theta) \\ \theta_0 + \theta &= \arccos\left(\frac{Z_0 + Z}{L_Z}\right) \end{aligned} \quad (3.9)$$

Therefore, the stroke from linear step motor, Y, can be calculated for desired Z position with the Eq 3.10 below.

$$\begin{aligned} Y_0 + Y &= L_Z \sin(\theta_0 + \theta) \\ Y &= L_Z \sin(\theta_0 + \theta) - Y_0 \end{aligned} \quad (3.10)$$

In case of Yaw axis, it's actuated by link connected to the motor with ball joint right below the Z frame, thus the variation of link length depending on the Z stroke needs to be considered. Following the notation in figure 3.12, the relation between angle and linear stroke of motor in Z axis which moves in parallel with Y axis can be described as follows. Let the L_θ and $L_{\theta Z}$ is the original and effective length of actuation link, the position Z determines this effective length $L_{\theta Z}$ as follows.

$$\begin{aligned} \theta_{\theta Z} &= \arcsin\left(\frac{Z}{L_\theta}\right) \\ L_{\theta Z} &= L_\theta \cos(\theta_{\theta Z}) \end{aligned} \quad (3.11)$$

To find θ_1 , the Yaw angle, the second cosine's law and trigonometric function is applied to for θ_2, φ and β with respect to the stroke from linear step motor, Yaw.

$$\begin{aligned}
\cos\theta_2 &= \frac{X^2 + (Y + Y_0)^2 - L_a^2 - L_{\theta Z}^2}{2L_a L_{\theta Z}} \\
\cos\varphi &= \frac{X^2 + (Y + Y_0)^2 + L_a^2 - L_{\theta Z}^2}{2L_a \sqrt{X^2 + (Y + Y_0)^2}} \\
\beta &= \text{atan}\left(\frac{Y + Y_0}{X}\right)
\end{aligned} \tag{3.12}$$

Finally, the Yaw angle, θ_1 , can be calculated with the Eq 3.13 in below.

$$\theta_1 = \beta - \varphi \tag{3.13}$$

3.3 Design and Mechanism of Scanner

3.3.1 Mechanism description

The scanner, angular measurement instrument, consists of 2 DOF manipulator and laser distance sensor from Keyence which has higher accuracy in micro meter level. The height between target object, peg or hole, is scanned along the surface of target object by utilizing the movement of manipulator and angle is calculated by applying trigonometric function to the height difference at each end and movement distance. Two external type of linear step motor are used for X and Z axis movement as shown in figure 3.13 with same lead size of ball screw, 0.635mm and linear modules are attached to the each of linear step motor to support the moment loads.

As pointed out in the previous section, the number of contact condition should be reduced to utilize the information from force sensor for estimating the error position efficiently. The three contact conditions out of five, made by angular errors, are concentrated around target position and no moments are generated on those conditions. Therefore, the scanner is attached next to the gripper and the angular error between peg and hole is measured after the plane contact made. The proposed scanner is chosen for angular measurement because it's superior to the vision which requires restricted condition on camera location and constraint on environment for achieving higher accuracy.

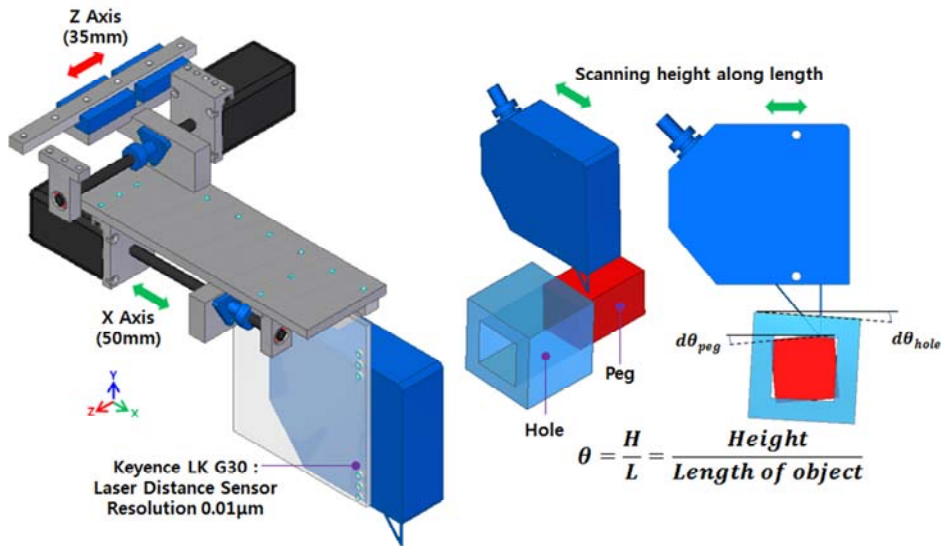


Figure 3.13 Schematics of scanner

3.3.2 FEM analysis for deflection compensation

The Finite Element Method (FEM) is applied to the scanner structure to check the deflection and straightness error while the distance sensor travels along the LM rail. The distance sensor is moving along LM rail which is attached to the cantilevered aluminum frame as shown in figure 3.14 and the deflection of frame induced by sensor position variation is inevitable. The laser distance sensor has high accuracy, 0.01µm level, but the deflection around 20 micro level induced by frame makes the accuracy of sensor degraded around this level.

To make use the sensor accuracy best, the compensation of frame deflection is required and simulation with FEM analysis is necessary to check rigidity of frame structure in initial design stage. To make FEM model on the scanner, cantilevered aluminum frame structure, nodes are assigned along the length of frame and the mass and stiffness matrix are generated with assigned number of nodes. After that, straightness error indicating the maximum deviation from reference model is calculated based on the deflection of frame from simulation results. The specific size and mass of aluminum frame and load condition of scanner indicated on figure 3.14 is used for FEM analysis.

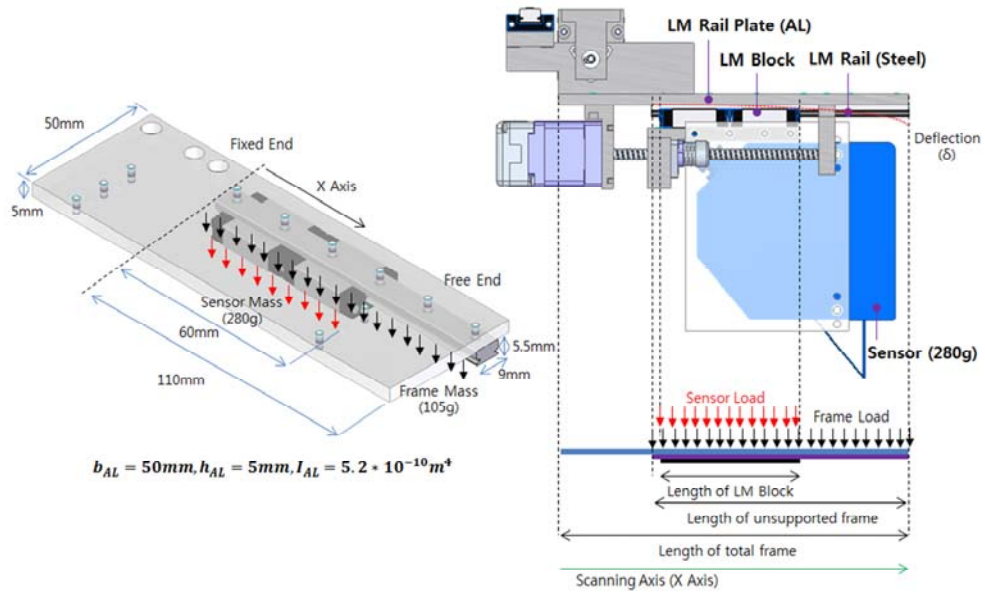


Figure 3.14 FEM model for scanner

The mass and stiffness matrix of aluminum frame divided by elements depending on the number of node is necessary for applying Finite Element Method and can be driven by cascading the consistent mass matrix and element stiffness matrix for each load conditions, axial force, torque and bending moment. To simulate the displacement on aluminum frame fully, the global mass and stiffness for every load conditions with 6 DOF should be defined and reflected to the model. However, it's reasonable to consider the only main load applied to the structure and displacement induced by that in terms of accuracy and computation time.

In case of cantilevered beam structure distance sensor is mounted on, force and the bending moment induced by unsupported frame and sensor weight cause the main deflection to the aluminum frame. Therefore, force and bending moment generated by its own weight and sensor position is only considered and reflected in the simulation model. The mass and stiffness matrix of the aluminum frame which describes the relationship between two forces, vertical gravity force and bending moment, and two deflections, deflection and deflected angle, with two degrees of freedom is driven as follows in Eq 3.14.

$$\begin{aligned}
M_{eq} &= M_{AL} \\
\frac{\rho A l}{420} \begin{bmatrix} 156 & 22l & 54 & -13l \\ 22l & 4l^2 & 13l & -3l^2 \\ 54 & 13l & 156 & -22l \\ -13l & -3l^2 & -22l & 4l^2 \end{bmatrix} & \begin{bmatrix} \textcircled{1} & & & \\ & 4 \times 4 & & \\ & & \textcircled{2} & \\ & & & \ddots \\ & & & & \textcircled{6} \end{bmatrix} \\
& \text{Mass Matrix } (2N) \times (2N) \\
\\
K_{eq} &= K_{AL} \\
\frac{EI}{l^3} \begin{bmatrix} 12 & 6l & -12 & 6l \\ 6l & 4l^2 & -6l & 2l^2 \\ -12 & -6l & 12 & -6l \\ 6l & 2l^2 & -6l & 4l^2 \end{bmatrix} & \begin{bmatrix} \textcircled{1} & & & \\ & 4 \times 4 & & \\ & & \textcircled{2} & \\ & & & \ddots \\ & & & & \textcircled{6} \end{bmatrix} \\
& \text{Stiffness Matrix } (2N) \times (2N) \\
\\
\frac{EI}{l^3} \begin{bmatrix} \begin{bmatrix} 12 & 6l & -12 & 6l \\ 6l & 4l^2 & -6l & 2l^2 \\ -12 & -6l & 12 & -6l \\ 6l & 2l^2 & -6l & 4l^2 \end{bmatrix} & & & \\ & \ddots & & \\ & & 0 & \\ & & & \begin{bmatrix} 12 & 6l & -12 & 6l \\ 6l & 4l^2 & -6l & 2l^2 \\ -12 & -6l & 12 & -6l \\ 6l & 2l^2 & -6l & 4l^2 \end{bmatrix} \end{bmatrix} \begin{bmatrix} \text{displacement of node 1} \\ \text{rotation of node 1} \\ \text{displacement of node 2} \\ \text{rotation of node 2} \\ \vdots \\ \text{displacement of node n} \\ \text{rotation of node n} \end{bmatrix}
\end{aligned} \tag{3.14}$$

Where, m = mass per unit length, l = unit length.

The simulation is executed with the boundary condition of cantilevered beam in which the degree of freedom at first node is eliminated. For the load conditions, its own frame weight and gravity force induced by sensor weight is considered and reflected in the model with the distributed force. In case of frame weight, the weight is distributed to the each node along 110mm aluminum frame length. The sensor weight, 280g, is also distributed along the 60mm length where two LM blocks supports the sensor. The overall load condition in each node, combining the both of the loads stated above, is computed in every position of sensor and applied to simulation. The figure 3.15 and 3.16 indicate the simulation results for deflection at frame when nodes are allocated by every 1mm along its length. Therefore, 111 nodes are assigned to the aluminum frame and weight of sensor is distributed to 61 nodes in the model. The deflection along the unsupported frame length, 110mm, depending on the sensor position is indicated in figure 3.15. It's clearly observed that the cantilevered aluminum beam deflects more as the sensor is positioned far from the origin and nonlinearly along its length. The deflection at the end of unsupported beam varies from $10\mu\text{m}$ to $27.3\mu\text{m}$ nonlinearly along the stroke of scanner in X axis, 50mm.

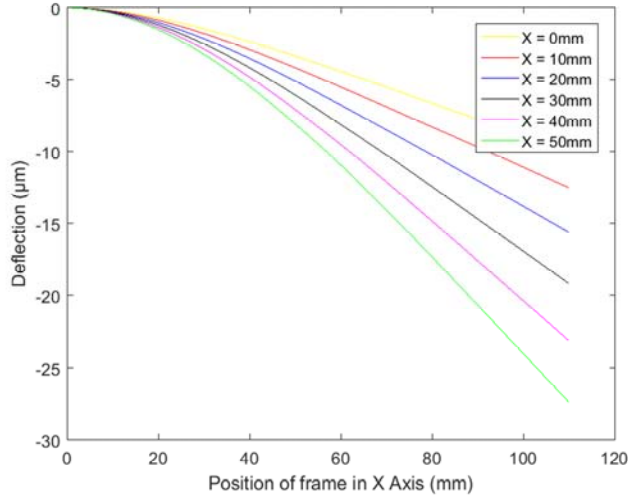


Figure 3.15 Deflection of frame depending on the position of sensor

The figure 3.16 indicates the deflection of sensor with respect to the sensor position and reference straightness line. It's clearly observed the sensor also deflects nonlinearly from 1.52μm to 17.64μm as it moves along the aluminum frame. The reference straightness line based on the deflection at each end point in figure 3.16 is,

$$\begin{aligned} \text{Reference Straight Line} = ax + b &= \frac{-17.64 + 1.523}{50 - 0}x - 1.523 \\ &= -0.3223x - 1.523 \end{aligned} \quad (3.15)$$

Based on the reference line found above, the straightness error defined in Eq 3.16 is calculated to estimate actual sensor accuracy. Even though the laser distance sensor has high accuracy around, 0.01μm level, this accuracy can't be available if the structure supporting the sensor transforms above this level. The deflection of sensor along its movement found above is 17.64μm, quite above the accuracy of sensor itself, thus it's necessary to use linear model to make use the accuracy best by compensating deflection.

$$\text{Straightness Error}(\delta) = \text{Reference}(x) - \text{deflection}(x) \quad (3.16)$$

The maximum straightness error along the position of sensor is 2.96 μm when sensor is positioned at 28mm. Therefore, the actual accuracy of the height measurement of scanner can be concluded as 3 μm.

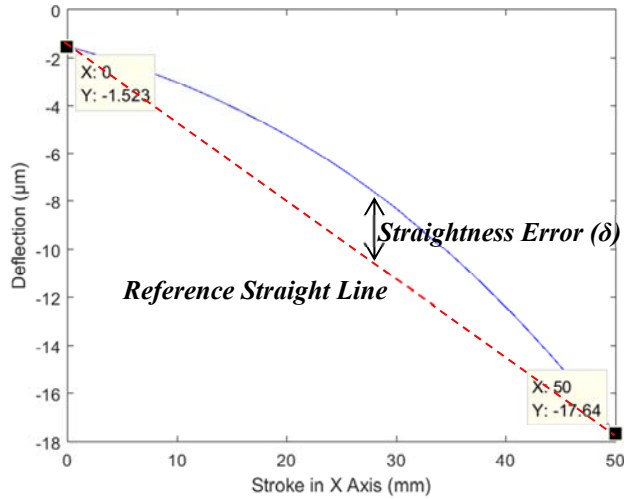


Figure 3.16 Deflection of sensor depending on the position of sensor

The modal analysis is also performed to check the mode shape and natural frequency of the structure. The figure 3.17 and table 3.1 indicates simulation results for the first five mode shapes and natural frequency of the cantilevered aluminum beam when 21 nodes are allocated along the frame length. The lowest natural frequency is 270Hz, quite above the frequency level from environment excitation, thus it can be concluded that the designed aluminum beam has enough rigidity to escape from the resonance.

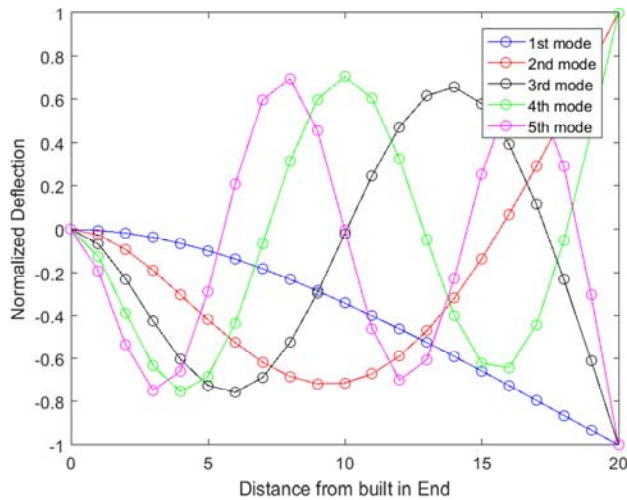


Figure 3.17 First five mode shapes of frame

Table 3.1 Natural frequency of cantilevered aluminum frame

| Mode | Natural Frequency (Hz) |
|-----------------|------------------------|
| 1 st | 270 |
| 2 nd | 1,697 |
| 3 rd | 4,751 |
| 4 th | 9,311 |
| 5 th | 15,395 |

Chapter 4

Error Recovery Algorithms

4.1 Clustering Algorithm for Error Estimation

Artificial intelligence, clustering the dataset consisted of position and reaction moment, is required to estimate the position error. As stated in previous section, the moment is generated on very restricted condition when there is position error only in one axis and this makes it necessary to measure the force data along the search area. Even after the angular alignment with the scanner, there still exist two cases in which no moment are generated in one of the cases thus clustering the dataset based on moment information is necessary to distinguish the position error between peg and hole. To use this condition for position error estimation, efficient algorithm is necessary to cluster the contaminated dataset. Theoretically, the moment generation only occurs simply when there is no position error in one axis as shown in figure 4.1. However, the actual measured force and moment data while it's moving is affected by inertia force and friction originated from the dynamic movement. Even more, the small compliance at the fingertip which is required for the friction generation for grasping object and prevention of jamming and wedging makes the generated force and moment deviated from the predicted one.

Depending on the approaches, the clustering algorithm is classified into non model based method represented by K means algorithm and model based method represented by Gaussian Mixture Model algorithm identifying the model parameters with the expectation maximization algorithm. Both of the approaches repeats the loop consisted of two phases, assigning dataset to cluster and re-computing the objective function, until it reaches optimized results satisfying the convergence constraint but working principle inside of the algorithm is different as follows.

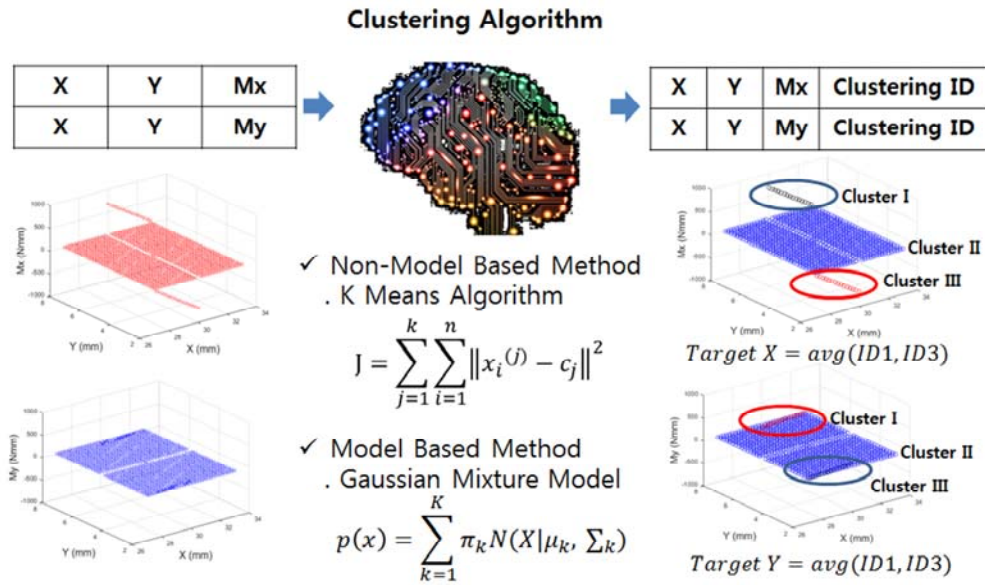


Figure 4.1 Clustering Algorithm for error recovery

4.1.1 K means algorithm

In case of K means algorithm, the optimization is executed on the multidimensional dataset with respect to minimizing the sum of distance between dataset and center of each cluster. Generally, it consists of two phases assigning dataset to cluster and computing the means of cluster and repeats until the data allocation to the given number of cluster does not change as described in figure 4.2.

K Means algorithm :

- Input : Dataset $\{x_1, x_2, x_3, \dots, x_{N-1}, x_N\}$, Number of Cluster (K)
- Output : Clustered Dataset, Center of each cluster

Initialize the center of each cluster

```
while(true) {
    for (i=1 to N)
        Assign the each data,  $x_i$ , to the close cluster
    for (j=1 to K)
        Compute the mean of clustered data
    if (No changes on allocation)
        break
}
```

Figure 4.2 Description of K Means Algorithm

Given the dataset, $\{x_1, x_2, x_3, \dots, x_{N-1}, x_N\}$, consisting of N observation of multidimensional variable x , and desired number of cluster, K , the objective function, J , to minimize for clustering dataset is,

$$J = \sum_{n=1}^N \sum_{k=1}^K r_{nk} \|x_n - \mu_k\|^2 \quad (4.1)$$

where, $r_{nk} = \begin{cases} 1 & \text{if } k = \arg \min_j \|x_n - \mu_j\| \\ 0 & \text{otherwise} \end{cases}$

$\mu_k = \text{center of cluster } k$

The r_{nk} is the binary indicator representing the cluster, K , the data, x_n , is assigned to and goal is to find the r_{nk} and μ_k which minimize the objective function, J . Taking the derivative objective function, J , with respect to μ_k gives,

$$2 \sum_{n=1}^N r_{nk} (x_n - \mu_k) = 0 \quad (4.2)$$

The objective function, J , is the quadratic function of μ_k , thus it's minimized when Eq 4.2 is zero. The center of cluster k , μ_k , can be calculated as follows.

$$\mu_k = \frac{\sum_n r_{nk} x_n}{\sum_n r_{nk}} \quad (4.3)$$

The binary indicator, r_{nk} , is recomputed and updated until it does not change.

4.1.2 Gaussian Mixture Model algorithm

In case of model based method, Gaussian Mixture Model used, the same number of Gaussian Model with the number of cluster is assigned to represent the dataset and the latent parameter is identified with expectation maximization algorithm as described in figure 4.3. It also consists of two phases assigning dataset to cluster and re-estimate the parameters on Gaussian Mixture Model and repeats until there are no changes on the estimated parameter to represent the model.

Gaussian Mixture Model algorithm :

- Input : Dataset $\{x_1, x_2, x_3, \dots, x_{N-1}, x_N\}$, Number of Cluster (K)
- Output : Clustered Dataset, Parameters on Gaussian Mixture Model

Initialize the parameters of Gaussian Mixture Model

```
while(true) {
    for (i=1 to N)
        Assign the each data,  $x_i$ , based on the probability model
    Re-estimate the parameters on Gaussian Mixture Model
    if (No changes on parameter estimation)
        break
}
```

Figure 4.3 Description of Gaussian Mixture Model Algorithm

The Gaussian Mixture Model which uses multiple number of Gaussian Model with linear superposition to represent the complex model can be described as follows.

$$p(x) = \sum_{k=1}^K \pi_k N(x|\mu_k, \Sigma_k)$$

where, K is the number cluster

(4.4)

π_k is the mixing coefficient for cluster k

μ_k is the mean of gaussian model for cluster k

Σ_k is the covariance of gaussian model for cluster k

Taking logarithm on both sides of Eq (4.4) gives,

$$\ln p(X|\pi, \mu, \Sigma) = \sum_{n=1}^N \ln \left\{ \sum_{k=1}^K \pi_k N(x_n|\mu_k, \Sigma_k) \right\} \quad (4.5)$$

The latent parameters on Gaussian Mixture Models in Eq (4.5) can be calculated by applying the expectation maximization algorithm which found the maximum likely solutions for model estimation. Taking first derivatives on Eq (4.5) with respect to μ_k, Σ_k , and setting to zero gives condition that should be satisfied for maximum likely hood estimation of μ_k, Σ_k and Eq (4.6) indicates derived equation for μ_k, Σ_k .

$$\begin{aligned}
\mu_k &= \frac{1}{N_k} \sum_{n=1}^N \gamma(z_{nk}) x_n \\
\Sigma_k &= \frac{1}{N_k} \gamma(z_{nk}) (x_n - \mu_k)(x_n - \mu_k)^T \\
N_k &= \sum_{n=1}^N \gamma(z_{nk}) \\
\gamma(z_{nk}) &= \sum_j \pi_j (x_n | \mu_j, \Sigma_j)
\end{aligned} \tag{4.6}$$

The last parameter, the mixing coefficient, π_k , can be calculated by finding one which maximize the quantity, $\ln p(X|\pi, \mu, \Sigma)$, with the constraint that sum of mixing coefficients is one. Reflecting this constraint with Lagrange Multiplier, the following Eq (4.7) is derived and used for estimation of mixing coefficient, π_k .

$$\ln p(X|\pi, \mu, \Sigma) + \lambda \left(\sum_{k=1}^K \pi_k - 1 \right) \tag{4.7}$$

The mixing coefficient for each of cluster is described in Eq (4.8) and can be viewed as the responsibility that each of cluster describe the observation, X.

$$\pi_k = \frac{N_k}{N} \tag{4.8}$$

4.2 Procedure for Error Recovery

The overall procedure for error recovery with the proposed gripper, scanner and clustering algorithm is described in figure 4.4. After the peg and hole make planar contact, the angular error between those is measured with scanner. The number of contact conditions, originally five, is reduced to two by angular aligning. However, there still exists one case in which no moment is generated, thus force and moment measurement with efficient trajectory minimizing the time for movement is required for position-moment map generation. To achieve this goal, the moment is measured

along the XY trajectory, which moves vertically and horizontally covering the given search area. The three dimensional dataset consisted of position of peg and moment information is generated for each position error estimation. For example, the dataset constructed with (x, y, M_x) and (x, y, M_y) is made and used for position error estimation in x and y axis respectively. After building up the dataset for given search area, the clustering algorithm well described above is applied to the dataset. Finally, the position error between peg and hole is extracted out after the clustering and the recovery is completed.

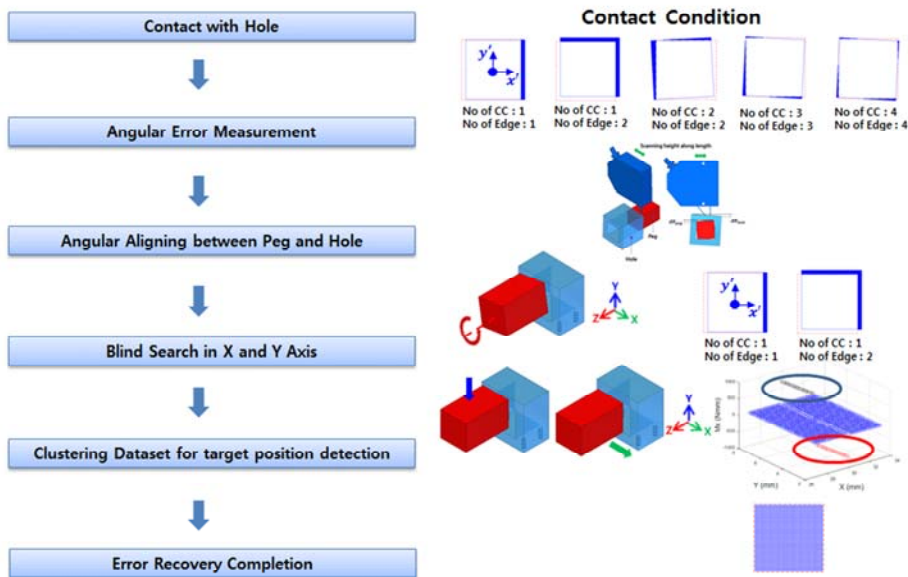


Figure 4.4 Flow chart for error recovery

4.3 Comparison of Error Recovery Algorithms

4.3.1 Comparison of trajectory in blind and XY search

The trajectory which takes the most of time for error recovery is one of the important factors in robotic assembly and is different from the way sensors are used. The blind search in which no sensors are used is simple but takes a lot of time for recovery because the trajectory needs to cover the all points in search area. Even more, the time for error recovery depending on the initial position error changes with it significantly.

As pointed out in the previous section, the redundancy in force-torque map makes it necessary to use sensors wisely for reducing the number of contact conditions. Adding sensors, scanner for angular alignment, can reduce the trajectory distance significantly while covering the same search area as with blind search. Generally, both of the position and angular error need to be compensated for successful assembly and the trajectory for each of error compensation with proposed system and algorithm for square Peg-In-Hole is compared with blind search in below.

4.3.2 Comparison of trajectory for position error recovery

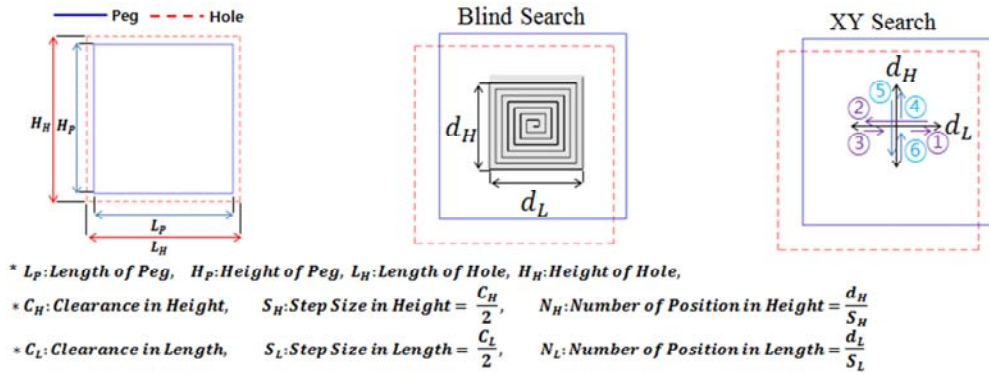


Figure 4.5 Trajectory for position error recovery

Given the clearance between peg and hole in length and height, the step size, the biggest allowable distance in one step movement not passing the target position for position error recovery is the half of the clearance as indicated in figure 4.5. The step size is same in both of blind search and XY search proposed here but the total number of step which determines the distance of trajectory is different from each other. In case of blind search, the trajectory covering the area determined by search distance, d_H and d_L , along height and length, is necessary for position error compensation whereas the trajectory only covering the double search distance is required in XY search. Let N_H and N_L be the number of position to check in height and length with given clearance and search distance. The trajectory in blind search is sum of the arithmetic series in height and length thus the total number of position to check in the blind search trajectory can be approximated as,

$$\sum 1 + 2 + \dots \frac{d_L}{S_L} + \sum 1 + 2 + \dots \frac{d_H}{S_H} = \frac{N_L(N_L + 1)}{2} + \frac{N_H(N_H + 1)}{2}$$

where, N_L : Number of Position in Length = $\frac{d_L}{S_L}$ (4.8)

N_H : Number of Position in Height = $\frac{d_H}{S_H}$

The trajectory in XY search consists of the horizontal and vertical line search which moves back and forth along moving direction as shown in figure 4.5 and the total number of position of check is,

$$2 \frac{d_L}{S_L} + 2 \frac{d_H}{S_H} = 2(N_L + N_H) \quad (4.9)$$

Summarizing the results above, the trajectory distance which is determined from the total number of position and step size is indicated on table 4.1 for both of blind and XY search method.

Table 4.1 Trajectory comparison of Blind Search and XY Search
for position error recovery

| | Blind Search | XY Search |
|----------------------------------|---|--|
| Distance to move for recovery | $\sum S_L(1 + 2 + \dots \frac{d_L}{S_L}) + \sum S_H(1 + 2 + \dots \frac{d_H}{S_H})$ $= S_L \frac{N_L(N_L + 1)}{2} + S_H \frac{N_H(N_H + 1)}{2}$ | $2d_L + 2d_H$ |
| Number of position to check | $\sum 1 + 2 + \dots \frac{d_L}{S_L} + \sum 1 + 2 + \dots \frac{d_H}{S_H}$ $= \frac{N_L(N_L + 1)}{2} + \frac{N_H(N_H + 1)}{2}$ | $2 \frac{d_L}{S_L} + 2 \frac{d_H}{S_H}$ $= 2(N_L + N_H)$ |

With the condition that search distance, d_H and d_L , and clearance, C_H and C_L , is same in height and length, the number of position to check in height and length, N_H and N_L , is same to each other. In this condition, the total number of position to check in trajectory of both of search method is summarized in table 4.2.

Table 4.2 Trajectory comparison of Blind Search and XY Search
when search distance and clearance is same in height and length

| | Blind Search | XY Search |
|--------------------------------|--------------|-----------|
| Number of position to check | $N(N + 1)$ | $4N$ |

In case of blind search, the total number of position to check is proportional to the squared N whereas that of XY search is proportional to quadruple N . Therefore, XY search is superior to the blind search by using short trajectory to cover same search area. Given the various values for search distance and clearance which determines the number of step to check, the total number of step in trajectory for both of method is tabulated on table 4.3. As shown below, trajectory distance of blind search increases drastically as with the number of step to move is increased whereas that of XY search is linearly proportional with the number of step to move. As the search area is increased and the clearance gets smaller, the number of steps to check along height and length are increased. Therefore, it can be concluded that the trajectory of XY search is superior to that of blind search in normal use condition which requires large search area with small clearance.

Table 4.3 Trajectory comparison of Blind Search and XY Search
with given search distance and clearance

| d | C | N | Number of Position to check | |
|----|-----|-----|-----------------------------|------------------------|
| | | | Blind Search (N_B) | XY Search (N_{XY}) |
| | | | $N_b(N_b + 1)$ | $4N_{xy}$ |
| 10 | 0.1 | 200 | 40,200 | 800 |
| 10 | 0.2 | 100 | 10,100 | 400 |
| 5 | 0.1 | 100 | 10,100 | 400 |
| 5 | 0.2 | 50 | 2,550 | 200 |

The coverable search area of both of method corresponding to the same number of position to check is also evaluated for comparison of trajectory. Following the notation on table 4.3, the total number of step in each method is,

$$\begin{aligned}
N_B &= N_b(N_b + 1) = \frac{2d_b}{C} \left(\frac{2d_b}{C} + 1 \right) \\
N_{xy} &= 4N_{xy} = 4 \frac{2d_{xy}}{C} = 8 \frac{d_{xy}}{C}
\end{aligned} \tag{4.10}$$

Equating both of equation in Eq 4.10 which describes the number of step in each method gives,

$$\begin{aligned}
\frac{2d_b}{C} \left(\frac{2d_b}{C} + 1 \right) &= 8 \frac{d_{xy}}{C} \\
4 \left(\frac{d_b}{C} \right)^2 + 2 \frac{d_b}{C} - 8 \frac{d_{xy}}{C} &= 0
\end{aligned} \tag{4.11}$$

Solving the second order equation above with respect to d_b gives the relationship between d_b and d_{xy} in both of method as follows.

$$d_b = \frac{C}{4} \left(-1 \pm \sqrt{1 + 32 \frac{d_{xy}}{C}} \right) \approx \frac{C}{4} \sqrt{32 \frac{d_{xy}}{C}} = \sqrt{2C d_{xy}} = \sqrt{2C} \sqrt{d_{xy}} \tag{4.12}$$

As shown in Eq 4.12, the search area in blind search, d_b , is square root of the product of clearance, C , and search area in XY search, d_{xy} . When the clearance is smaller than 0.5mm, the search area of the blind search is always smaller that of XY search. Therefore, inferiority of the blind search to XY search can be verified with the above equation and this becomes clearer as the clearance between mating parts gets smaller.

4.3.3 Comparison of trajectory for angular error recovery

In addition to the trajectory for position error, the trajectory for angular error compensation is necessary for complete Peg-In-Hole task. The blind search needs to add additional trajectory into the position error trajectory described above for angular error compensation. Therefore, the trajectory for angular error should be added to the every position in position error trajectory as shown in figure 4.6 and this waste a lot of time in recovery. In contrast to that, the scanner reduces wastes on the trajectory distance by measuring the angular error actively. The height along predefined three positions is only measured with determined trajectory thus the no wastes exist on the

trajectory. Even more, relatively longer distances between three points make it possible to use higher velocity during movement. The comparison of angular trajectory for both of method is summarized on table 4.4.

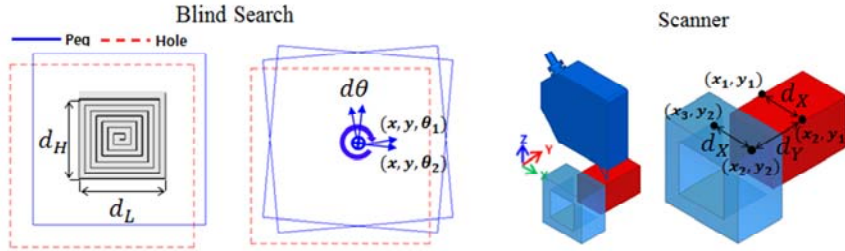


Figure 4.6 Trajectory for angular error recovery

Table 4.4 Trajectory comparison of Blind Search and XY Search for angular error compensation

| | Blind Search | Scanner |
|-------------------------------|---------------------|--------------|
| Distance to move for recovery | $N_B \cdot d\theta$ | $2d_X + d_Y$ |
| Number of position to check | N_B | 3 |

* N_B (Number of steps required for given searching area) = $N(N + 1)$, $N = \frac{2d}{c}$

4.3.4 Comparison of variation in recovery time

In addition to the time for error recovery, the variation of it is also important factor to consider for practical use because it's hard to use if the time for error recovery varies drastically depending on the specific condition. The recovery through blind search has weakness in this point because the recovery time depends on the initial position error between peg and hole. Table 4.5 indicates the variation in number of steps for position error recovery in both of method with various given parameters, clearance and search distance. As the total number of step, N , is increased, the variation of the recovery in blind search which can be represented by standard deviation is increased proportionally with squared N whereas proposed XY search has no variation on it.

Table 4.5 Variation of recovery time in Blind Search and XY Search
for position error compensation

| d | C | N | Variation in number of steps for position error recovery | | | |
|----|-----|-----|--|--------|--------|-----------|
| | | | Blind Search | | | XY search |
| | | | Max | Mean | STD | Nominal |
| 10 | 0.1 | 200 | 39,601 | 19,668 | 11,477 | 800 |
| 10 | 0.2 | 100 | 9,801 | 4,834 | 2,851 | 400 |
| 5 | 0.1 | 100 | 9,801 | 4,834 | 2,851 | 400 |
| 5 | 0.2 | 50 | 2,401 | 1,168 | 703 | 200 |

Although blind search use deterministic trajectory for covering predefined search area, the recovery time varies with the initial position error severely as shown in figure 4.7 representing the last case on table 4.5. This is one of the other reasons why appropriate sensor use, scanner proposed here, is necessary for robust error estimation time.

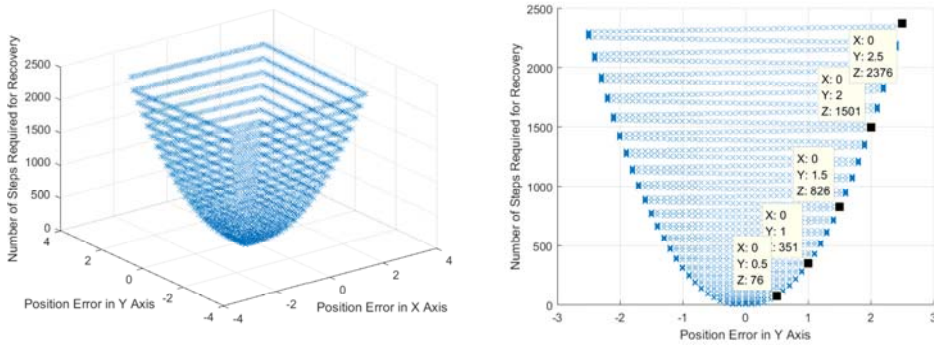


Figure 4.7 Variation in number of step for position error recovery
ISO View (Left), Front View (Right)

Chapter 5

Experimental Results

5.1 Angular Error Measurement of Scanner

5.1.1 Verification of scanner accuracy and repeatability

The accuracy and repeatability of angle measurement from scanner is tested and verified with the experiment. The accuracy degradation induced from the frame deflection is already pointed out in the previous section and it's verified that it can be minimized with compensation with straight line model. The overall accuracy and repeatability of measurement depends on start and end position of scanner because the reference line used for model is estimated with these two points. Considering all of these, the height of each end point is set to same level initially and the accuracy and repeatability of the scanner is tested with following experimental setup.

To give the exact reference angle for measurement, the rotation stage in which rotation angle is controlled by micrometer head is used for experiment. The specification of rotation stage, RTSS 40 form Misumi, is described in figure 5.1. The square plate with the size of 40mm is rotated by turning the micrometer head and the working range and resolution in angle micrometer tab makes is $\pm 10^\circ$ and $1'51'' (\approx 0.03^\circ)$ respectively.

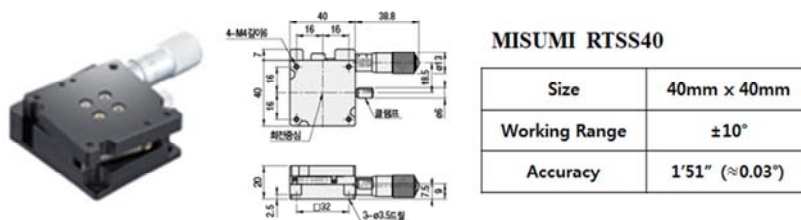


Figure 5.1 Specification of rotation stage, RTSS40

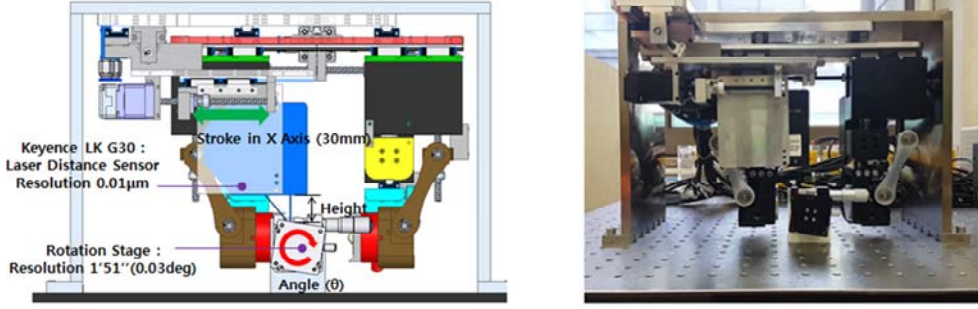


Figure 5.2 Experimental setup for angle measurement of scanner
Schematic of setup (Left) and Actual experimental setup (Right)

The rotation stage, RTSS40, is installed below the scanner as shown in figure 5.2 and the height between sensor and stage along the top surface of stage is measured. While moving 30mm along top surface, the height corresponding to rotation stage angle is measured for three times and the transformed results, measured angles, are summarized in table 5.1. The accuracy and repeatability of angle measurement depends on position accuracy and repeatability of 2DOF manipulator in scanner and ISO standard 9283 which describes performance criteria and related test methods for manipulating industrial robots is applied for the analysis. The position accuracy, a_p , defined as the distance between the commanded position, X_{cmd} , and mean of measured position, X_{avg} is,

$$a_p = \|X_{avg} - X_{cmd}\| = \sqrt{(\bar{x} - x_{cmd})^2 + (\bar{y} - y_{cmd})^2 + (\bar{z} - z_{cmd})^2} \quad (5.1)$$

The position repeatability, σ_p , defined as the standard deviation of the N repeated position measurement is,

$$\sigma_d = \sqrt{\frac{\sum_{i=1}^N (X_i - \bar{X})^2}{N - 1}} \quad (5.2)$$

Following the definition described above, the position accuracy and repeatability can be represented as deviation of mean position from commanded position and radius of circle as shown in figure 5.3. The worst-case deviation which indicates the maximum deviation from commanded position can be calculated with both of accuracy and repeatability of measurement.

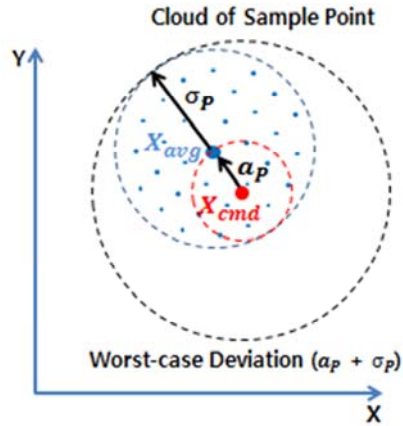


Figure 5.3 Description for position accuracy and repeatability

The calculated accuracy, repeatability and worst case deviation of measurement for each commanded rotation stage angle are tabulated in table 5.1. The maximum measurement error among commanded 13 stage angles, represented with the worst-case deviation which is defined with position accuracy and repeatability, is 0.087 degree. Therefore, it's verified that the scanner has the required accuracy (<0.1 degree) in angle measurement and is applicable to the angular error measurement for peg in hole task through experiment.

Table 5.1 Accuracy, repeatability and worst-case deviation of scanner measurement

| Stage Angle (deg) | Measured Angle (deg) | | | Average (X_{avg}) (deg) | Accuracy (a_p) (deg) | Repeatability (σ_p) (deg) | Worst Case Deviation (deg) |
|-------------------|----------------------|--------|--------|-----------------------------|--------------------------|------------------------------------|----------------------------|
| | 1st | 2nd | 3rd | | | | |
| 0.46 | 0.483 | 0.490 | 0.491 | 0.488 | 0.028 | 0.005 | 0.033 |
| 0.37 | 0.356 | 0.388 | 0.363 | 0.369 | -0.001 | 0.017 | -0.018 |
| 0.28 | 0.257 | 0.313 | 0.292 | 0.288 | 0.008 | 0.028 | 0.036 |
| 0.19 | 0.212 | 0.193 | 0.199 | 0.201 | 0.011 | 0.010 | 0.021 |
| 0.09 | 0.125 | 0.130 | 0.035 | 0.097 | 0.007 | 0.050 | 0.057 |
| 0 | 0.065 | -0.051 | -0.015 | 0 | 0 | 0.059 | 0.059 |
| -0.09 | -0.076 | -0.091 | -0.132 | -0.010 | -0.1 | 0.029 | -0.039 |
| -0.19 | -0.187 | -0.133 | -0.211 | -0.177 | 0.013 | 0.040 | 0.053 |
| -0.28 | -0.285 | -0.258 | -0.287 | -0.276 | 0.004 | 0.016 | 0.020 |
| -0.37 | -0.344 | -0.354 | -0.356 | -0.351 | 0.016 | 0.006 | 0.022 |
| -0.46 | -0.431 | -0.477 | -0.371 | -0.426 | 0.034 | 0.053 | 0.087 |

The overall accuracy and repeatability of measurement is also calculated with the measurement error which gives larger population for estimating the probability distribution model. Base on this, the worst-case deviation in 3σ level which represents the 99.7% probability distribution is also calculated for the analysis of measurement accuracy. The table 5.2 below indicates the calculated error of each measurement with the measured angle.

Table 5.2 Measurement error of scanner

| Stage Angle (deg) | Measurement Error (Measured Angle) (deg) | | |
|-------------------|--|---------------|---------------|
| | 1st | 2nd | 3rd |
| 0.46 | 0.02 (0.48) | 0.03 (0.49) | 0.03 (0.49) |
| 0.37 | -0.02 (0.35) | 0.01 (0.38) | -0.01 (0.36) |
| 0.28 | -0.03 (0.25) | 0.03 (0.31) | 0.01 (0.29) |
| 0.19 | 0.02 (0.21) | 0.00 (0.19) | 0.00 (0.19) |
| 0.09 | 0.03 (0.12) | 0.04 (0.13) | -0.06 (0.03) |
| 0 | 0.06 (0.06) | -0.05 (-0.05) | -0.01 (-0.01) |
| -0.09 | 0.02 (-0.07) | 0.00 (-0.09) | -0.04 (-0.13) |
| -0.19 | 0.01 (-0.18) | 0.06 (-0.13) | -0.02 (-0.21) |
| -0.28 | 0.00 (-0.28) | 0.03 (-0.25) | 0.00 (-0.28) |
| -0.37 | 0.03 (-0.34) | 0.02 (-0.35) | 0.02 (-0.35) |
| -0.46 | 0.03 (-0.43) | -0.01 (-0.47) | 0.09 (-0.37) |

The figure 5.4 indicates the histogram of 33 measurement error tabulated in table 5.2 and it can be clearly observed that measurement follows the normal distribution. The calculated mean, standard deviation and worst-case deviation in 3σ level of measurement error are indicated in table 5.3 below.

Table 5.3 Analysis of measurement error

| | |
|--|----------|
| Mean (\bar{E}) | 0.01 deg |
| Standard Deviation (σ_E) | 0.03 deg |
| Worst-case deviation ($\bar{E} \pm 3\sigma_E$) | 0.1 deg |

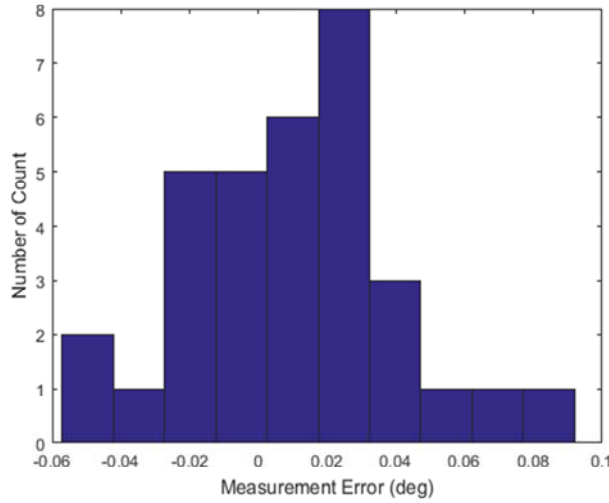
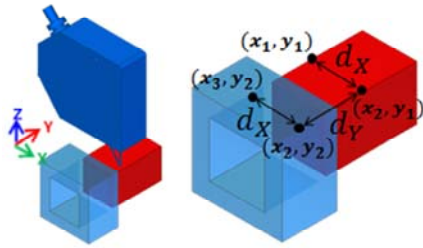


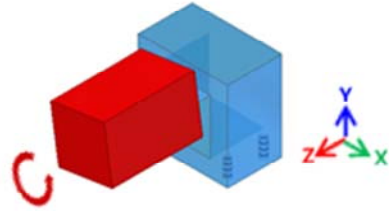
Figure 5.4 Histogram for measurement error

5.1.2 Measurement and alignment of angular error

The angular error measurement between peg and hole is executed after plane contact is made and alignment is carried out with finger manipulation as shown in figure 5.5. For stable grasping and making complete plane contact, the small compliance at the fingertip is required for friction and passive alignment which is necessary for successful assembly and manipulation of peg. In addition to that, small compliance is also helpful in preventing the conditions of jamming and wedging during insertion. However, the compliance at the tip is not good for position estimation because position and orientation of peg is changed even with the small force applied to it. Therefore, it's reasonable to measure the angular error after the complete plane contact between peg and hole is made and there's no change on angular error. After the plane contact is made, the scanner follows the trajectory passing through the predefined four points along the top surface of peg and hole. Then, the each angle of peg and hole is calculated with measured height from scanner and angular error between peg and hole is extracted out. Finally, the peg is manipulated with two fingers and alignment with hole is completed. The procedure executed by the scanner and gripper prototype is well described on the figure 5.5 below.



(Angular Error Measurement)



(Angular Error Alignment)

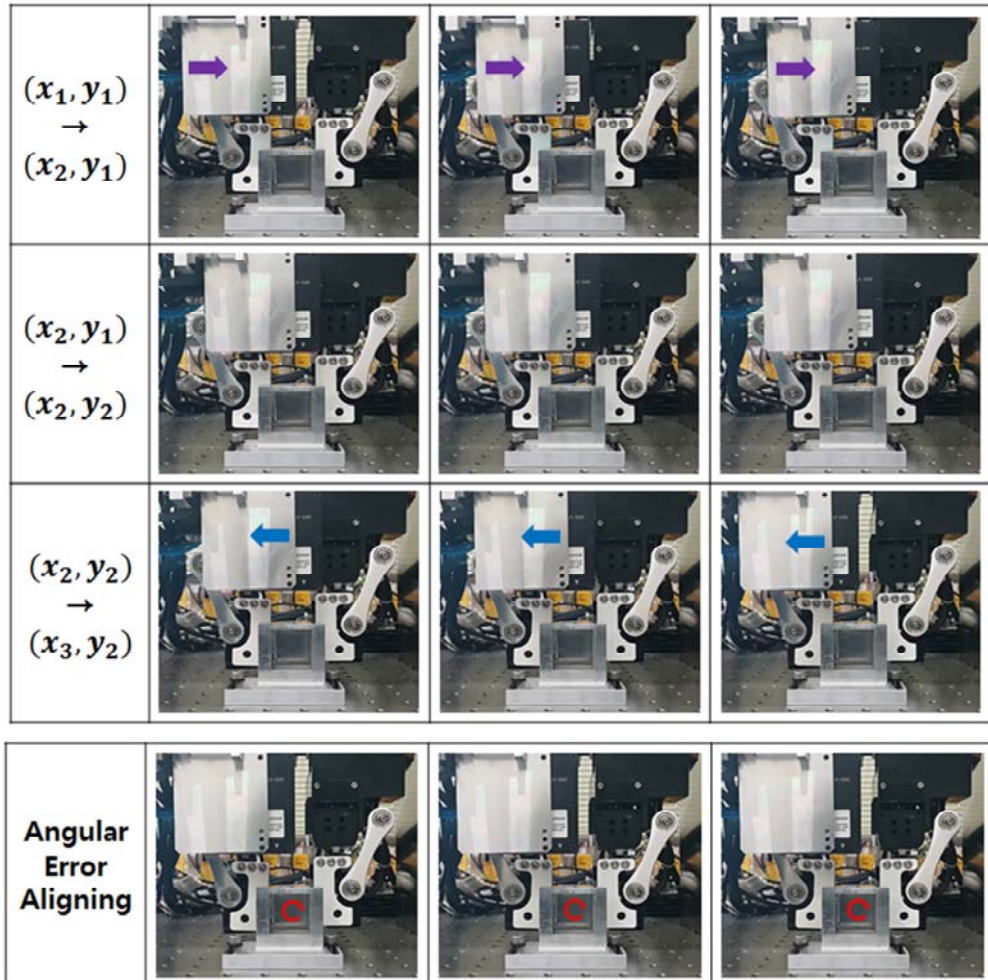


Figure 5.5 Measurement and alignment of angular error with scanner and gripper

5.2 Reaction Moment Measurement at Fingertip

5.2.1 Measurement of moment data

The reaction moment is measured along the predefined XY trajectory peg follows and the position errors are extracted out by clustering measured dataset consisted of the peg position and measured force. The actual position of peg, mean position of two fingers, is calculated with feedback position of two fingers. The figure 5.6 indicates the actual force measurement with gripper prototype and trajectory it follows when position error between peg and hole is set to 1.5mm in each axis respectively. After angular alignment, there still exist two contact conditions and moments are generated in only one of contact conditions. The XY trajectory covering the search area with horizontal and vertical line movement consists of 3 line movements in each axis. Manipulation of peg with prototype gripper while it moves 6mm in each axis is well described in figure 5.6 below.

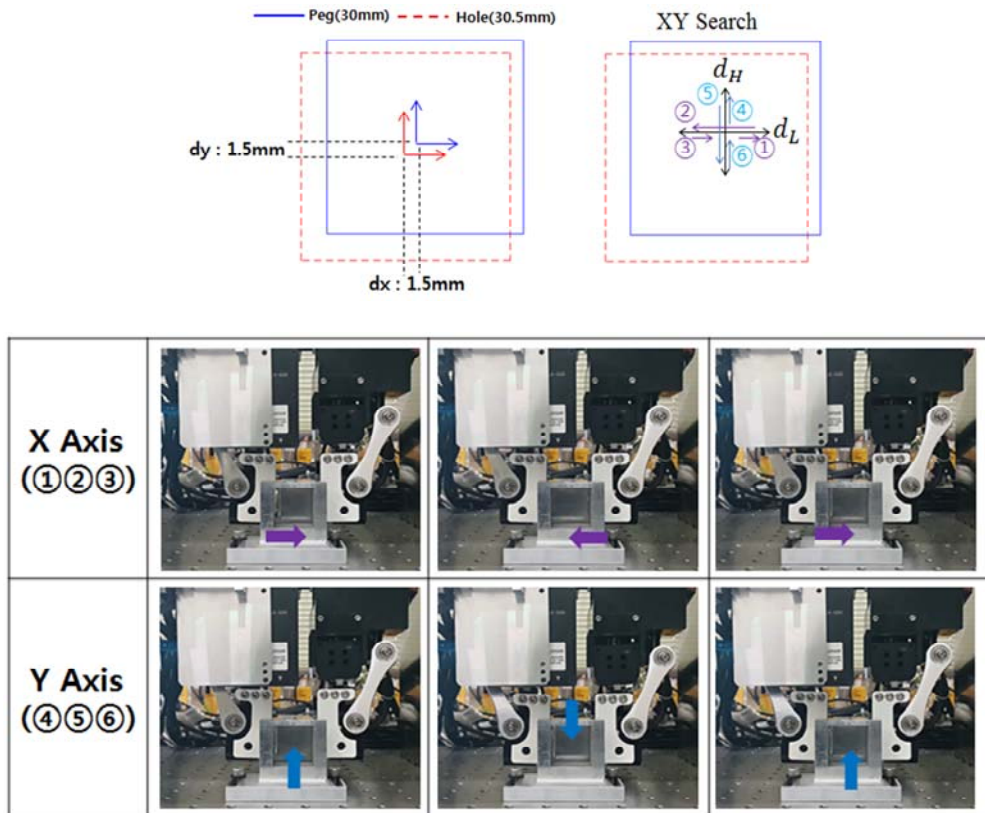


Figure 5.6 Measurement of force data with given position error along XY trajectory

5.2.2 Description of measurement condition

The peg and hole with the square size of 30 and 30.5mm is used and set up with position error of 1.5mm in each x and y axis for the experiments as shown in figure 5.6. The initial position error between peg and hole is given for verification of error estimation from clustering and measured with steel ruler after making plane contact and set to target value, 1.5mm, with manipulation of fingers. The force and moment at each finger holding the peg is measured along the XY trajectory constructed with search distance, d_H and d_L , of 6mm in each axis respectively. Then, the force and moment acting on the peg is measured and used for building up dataset for both of clustering algorithm described above to estimate the position error.

The XY trajectory with three different maximum velocities, 1, 2 and 5mm/sec is used to check the robustness of the clustering algorithm to movement velocity which influences on measured dataset used for clustering. The figure 5.7 indicates the three actual position and velocity profiles used in the experiment. The maximum velocity used in the experiment is set to 5mm/sec in each axis because the lead of ball screw, very small as 0.635mm, makes it restricted. It's observed that the peg follows the command position very well regardless of the maximum velocity although it deviates from commanded velocity more as the maximum velocity is increased.

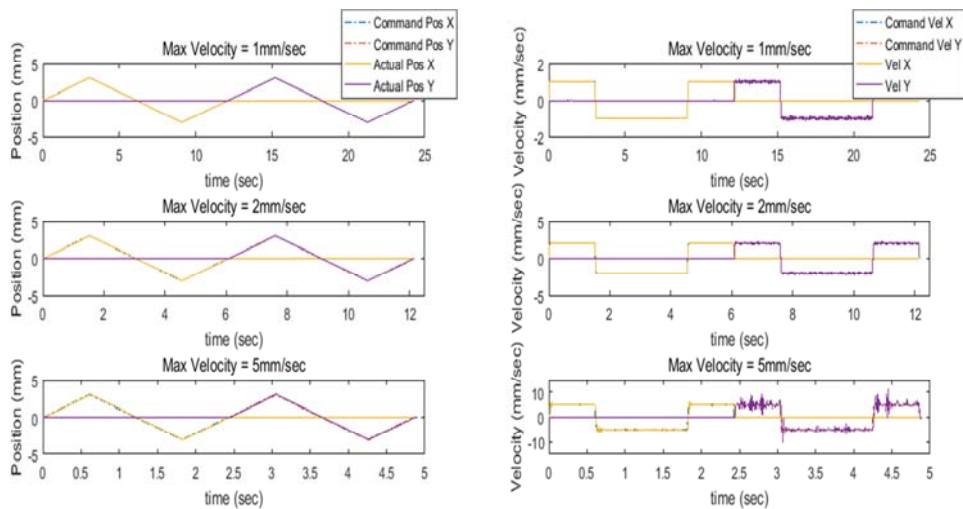


Figure 5.7 Actual position and velocity in XY trajectory depending on max velocity 1mm/sec (Top), 2mm/sec (Middle), 5mm/sec (Bottom)

The insertion force and reaction moment on peg along the each of horizontal and vertical movement in XY trajectory with 5mm/sec velocity is indicated in figure 5.8. The insertion force is indicated in blue line and both of the moments in each axis are indicated in red line. It's clearly observed that the moments are generated around both of given error position in each axis. However, the range of moment generation is bigger than 0.5mm, expected range based on clearance between peg and hole. The compliance in each fingertip cause this range widened to around 2mm.

The insertion force indicating the contact force between peg and hole is controlled in pneumatic way with same pressure. The mean values of insertion forces along both of horizontal and vertical movement were -16.23N and -15.64 respectively, almost same level in both of cases, but it fluctuates more in horizontal movement. In case of horizontal movement, it varies from -19.28N to -12.96N whereas it varies from -17.46N to -13.66N in vertical movement. The effective compliance of peg is determined from compliance model at the fingertip. Even though both of cases have same contact condition defined in section 2, the cross section areas supporting insertion force at the fingertip is different. While peg moves vertically, compliance at right finger is fully constrained. This leads to more rigidity in structure at fingertip surrounding the peg and less variation on insertion force. Both of clustering algorithm, K means and Gaussian Mixture Model algorithm, are applied to the measured each of dataset and the results for estimated error are described in below.

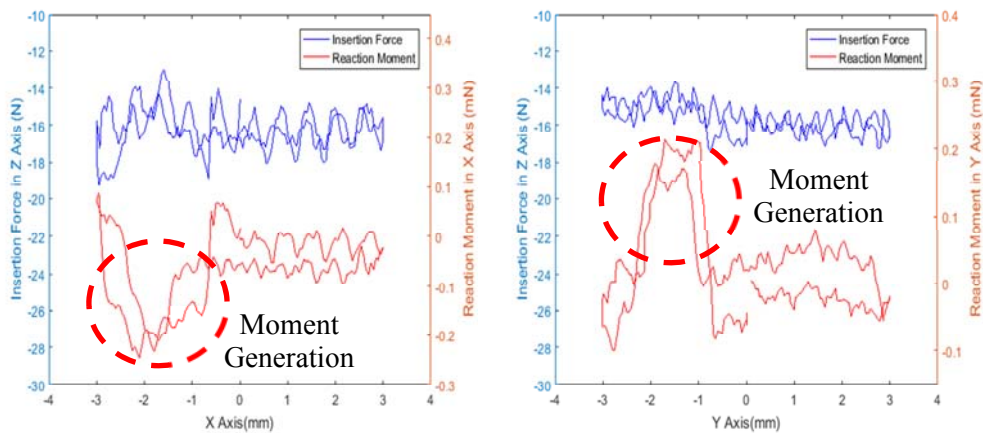


Figure 5.8 Insertion force and moment when max velocity = 5mm/sec
Moment in x axis (Left), Moment in y axis(right)

5.2.3 Clustering results from K means algorithm

Applying the K means algorithms on the dataset above gives the clustering results for error estimation. As shown in figure 5.9, both of dataset are classified into two clusters and the estimated position error in x and y axis is -1.79mm and -1.49mm respectively. The maximum error between estimated and given position error is 0.29mm. Although the range of moment generation is increased due to the compliance at the fingertip as pointed out, it's verified through K means algorithm that distribution of it is centered at given position error. Therefore, the compliance inducing the increased range of moment generation makes no problems in error estimation and advantages of it can be utilized for small passive alignment.

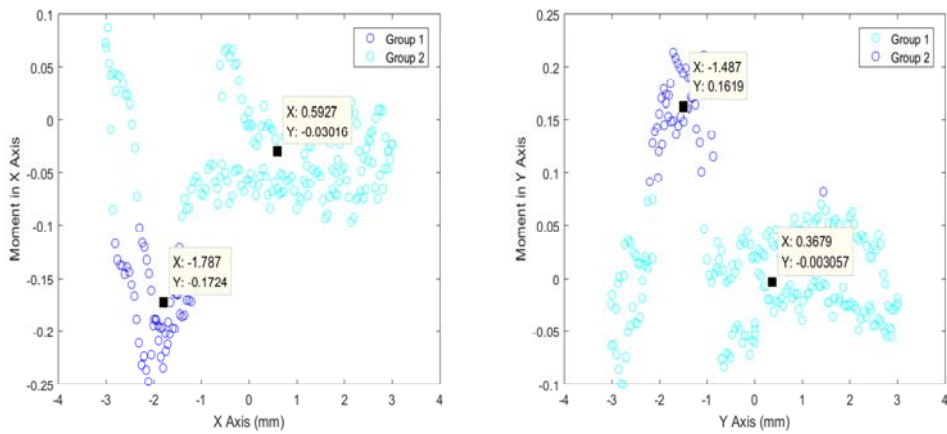


Figure 5.9 Clustering results with k means algorithm when max velocity = 5mm/sec
Moment in x axis (Left), Moment in y axis(right)

To check the robustness of force measurement and error estimation, the force and moment is measured three times in same conditions, given position error of 1.5mm in each axis and maximum velocity of 5mm/sec, and position error is estimated for each dataset. The figure 5.10 and table 5.4 indicates the clustering result with k means algorithm and summary of clustered dataset. The averaged position errors in x and y axis are -1.76mm and -1.49mm and maximum difference among three estimated position errors in x and y axis are 0.05mm and 0.14mm. The measured moment in each dataset also shows same patterns and magnitude along the horizontal and vertical movement. Therefore, it's verified through experiments that measurement at the fingertip and error estimation with K means algorithm has robustness by creating same result for position error estimation.

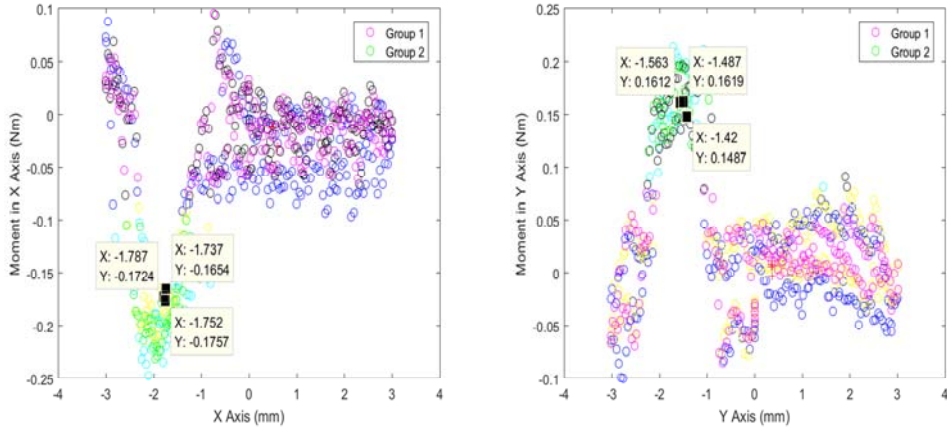


Figure 5.10 Clustering results with k means algorithm on three datasets measured from same condition, Moment in x axis (Left), Moment in y axis(right)

The clustering results of each dataset with K means algorithm also shows same patterns with the similar number of data allocation to cluster in which moment is generated. Almost same percentage of data in each dataset around 23% and 20%, is assigned to the moment generated cluster as shown in table 5.4. Among the 246 total data on average, the 57 and 49 data are allocated to the moment generated cluster in each x and y axis respectively.

Table 5.4 Clustering results with k means algorithm on three datasets measured from same condition

| Test No | Position Error in X Axis | | | Position Error in Y Axis | | |
|-----------------|--------------------------|-------------|----------------------|--------------------------|-------------|---------------------|
| | Number of Data | | Estimated Error (mm) | Number of Data | | Estimated Error(mm) |
| | Total | Cluster I | | Total | Cluster I | |
| 1 st | 245 | 61 (25%) | -1.787 | 245 | 49 (20%) | -1.487 |
| 2 nd | 247 | 56 (23%) | -1.737 | 247 | 51 (21%) | -1.420 |
| 3 rd | 246 | 55 (22%) | -1.752 | 246 | 47 (19%) | -1.563 |
| Average | 246 | 57 (23%) | -1.760 | 246 | 49 (20%) | -1.490 |
| Max difference | 2 | 6 | 0.05 | 2 | 4 | 0.14 |

The force and moment data is measured with three different velocities, 1, 2 and 5mm/sec, and same initial position error of 1.5mm in each axis along XY trajectory to check the robustness of the clustering algorithm to movement velocity which influences on measured dataset used for clustering. The figure 5.11 and table 5.5 indicates the clustering result of these three dataset with k means algorithm and summary of clustered dataset.

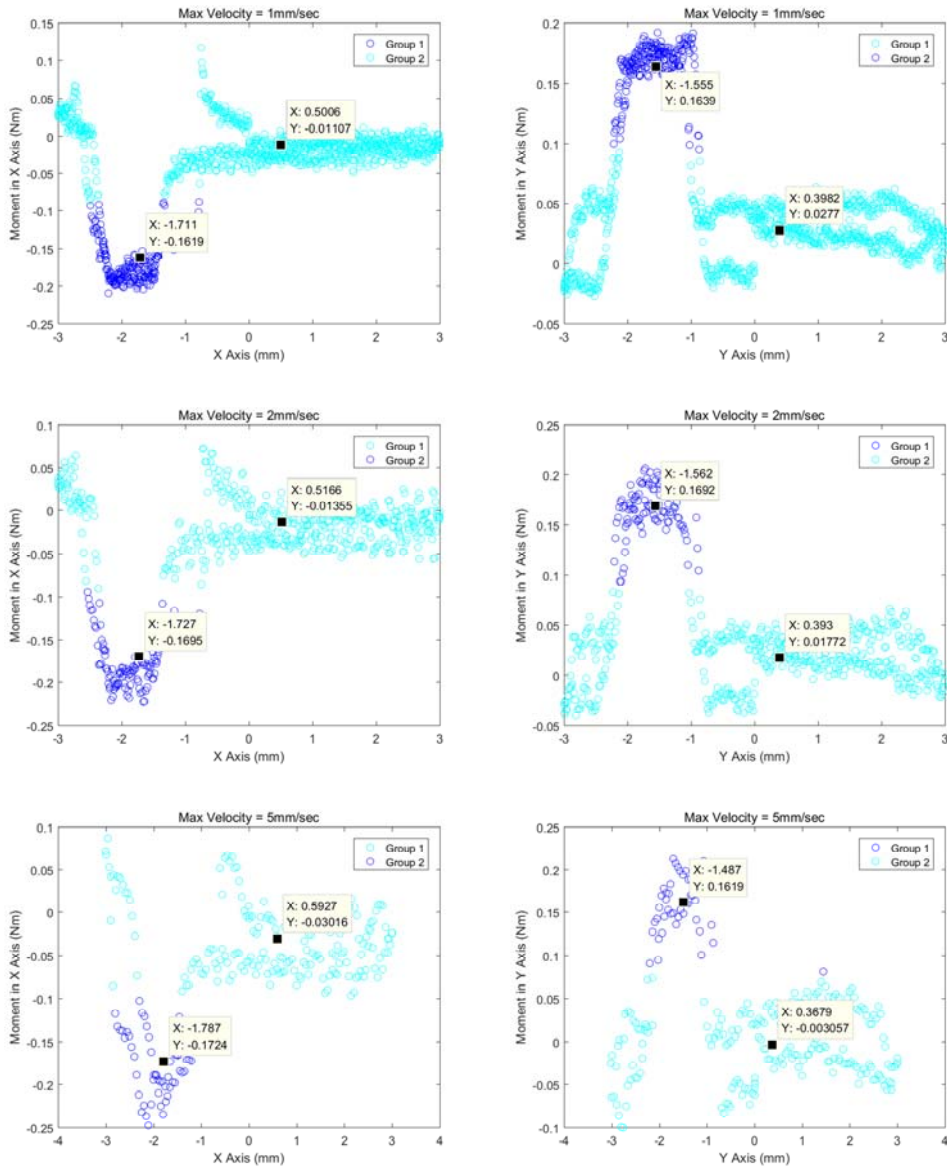


Figure 5.11 Clustering results with k means algorithm on three datasets measured from different velocity, 1mm/sec (Top), 2mm/sec (Middle), 5mm/sec (Bottom)

As shown above, the moment along horizontal and vertical movement shows same pattern and magnitude regardless of the velocity while the total number of data in dataset is decreased with increased velocity. The estimated mean position error in x and y axis are -1.74mm and -1.53mm and maximum difference among three estimated position errors in x and y axis are 0.08mm. Therefore, it can be concluded that the K means algorithm have robustness to the certain level of velocity in XY trajectory.

Although the number of total data in each dataset is decreased proportionally with increased velocity, clustering of each dataset allocates the number of data with same percentage in each dataset to moment generated region. Almost same percentage of data in each dataset around 24% and 20%, is assigned to the moment generated cluster as shown in table 5.5.

Table 5.5 Clustering results with k means algorithm on three datasets measured from different velocity

| Velocity | Position Error in X Axis | | | Position Error in Y Axis | | |
|----------------|--------------------------|--------------|----------------------|--------------------------|--------------|----------------------|
| | Number of Data | | Estimated Error (mm) | Number of Data | | Estimated Error (mm) |
| | Total | Cluster I | | Total | Cluster I | |
| 1mm/sec | 1,215 | 275 (23%) | -1.711 | 1,215 | 247 (20%) | -1.555 |
| 2mm/sec | 608 | 140 (23%) | -1.727 | 608 | 122 (20%) | -1.562 |
| 5mm/sec | 245 | 61 (25%) | -1.787 | 245 | 49 (20%) | -1.487 |
| Average | - | - | -1.741 | - | - | -1.534 |
| Max difference | - | - | 0.076 | - | - | 0.075 |

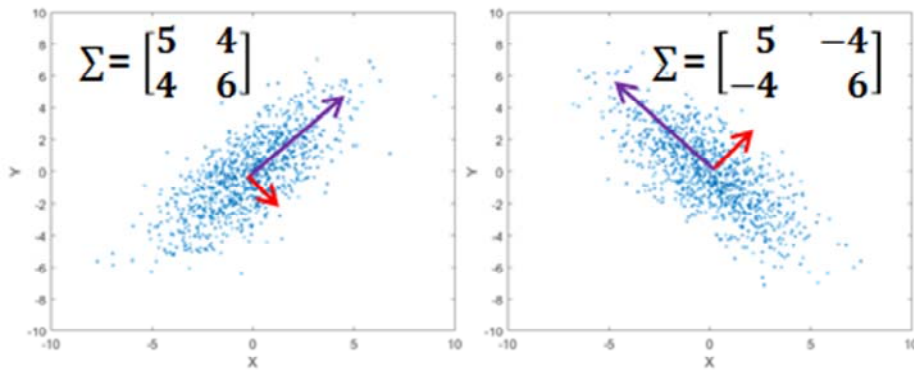
5.2.4 Clustering results from Gaussian Mixture Model algorithm

Applying Gaussian Mixture Model algorithm on the same dataset represented in figure 5. 10 which is measure with given position error of 1.5mm in each axis and maximum velocity of 5mm/sec, the clustered results for each dataset is indicated in figure 5.13. It's clearly observed the cluster results are categorized into two cases in both of moment dataset. In case of Gaussian Mixture Model algorithm, the parameters in the Gaussian model, mean and covariance, are identified with expectation maximization.

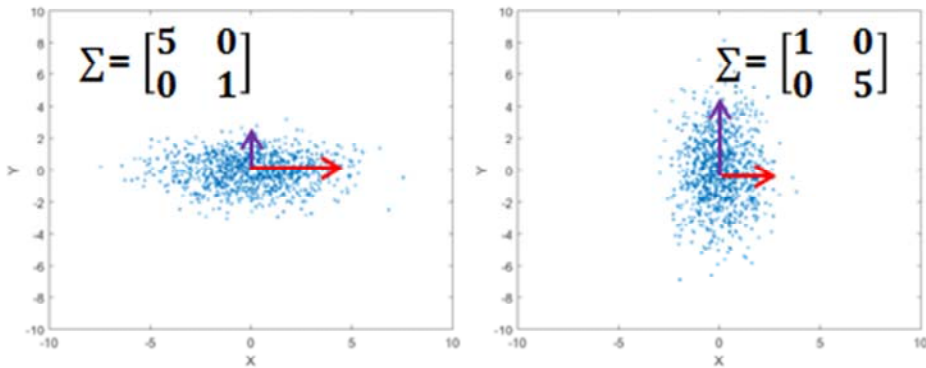
Depending on the covariance matrix of cluster assigned for error estimation, the shape of distribution is determined thus the different clustering results come out.

Covariance matrix indicates whether the relationship between two joint variables is strong or weak and this relationship significantly influence on the shape of distribution. The representative distribution of two joint variables depending on the covariance matrix is indicated in figure 5.12 below.

$$\text{cov}(X, Y) = E[(X - E[X])(Y - E[Y])] = \Sigma = \begin{bmatrix} \sigma(x, x) & \sigma(x, y) \\ \sigma(y, x) & \sigma(y, y) \end{bmatrix} \quad (5.3)$$



Distribution with covariance matrix of strong relationship



Distribution with covariance matrix of weak relationship

Figure 5.12 Distribution of joint variables depending on covariance matrix

When the covariance matrix with strong relationship is assigned, the principle axis of distribution is inclined with respect to horizontal or vertical axis. When the covariance matrix with weak relationship, diagonal type, is assigned, the principle axis of distribution is parallel with respect to horizontal or vertical axis.

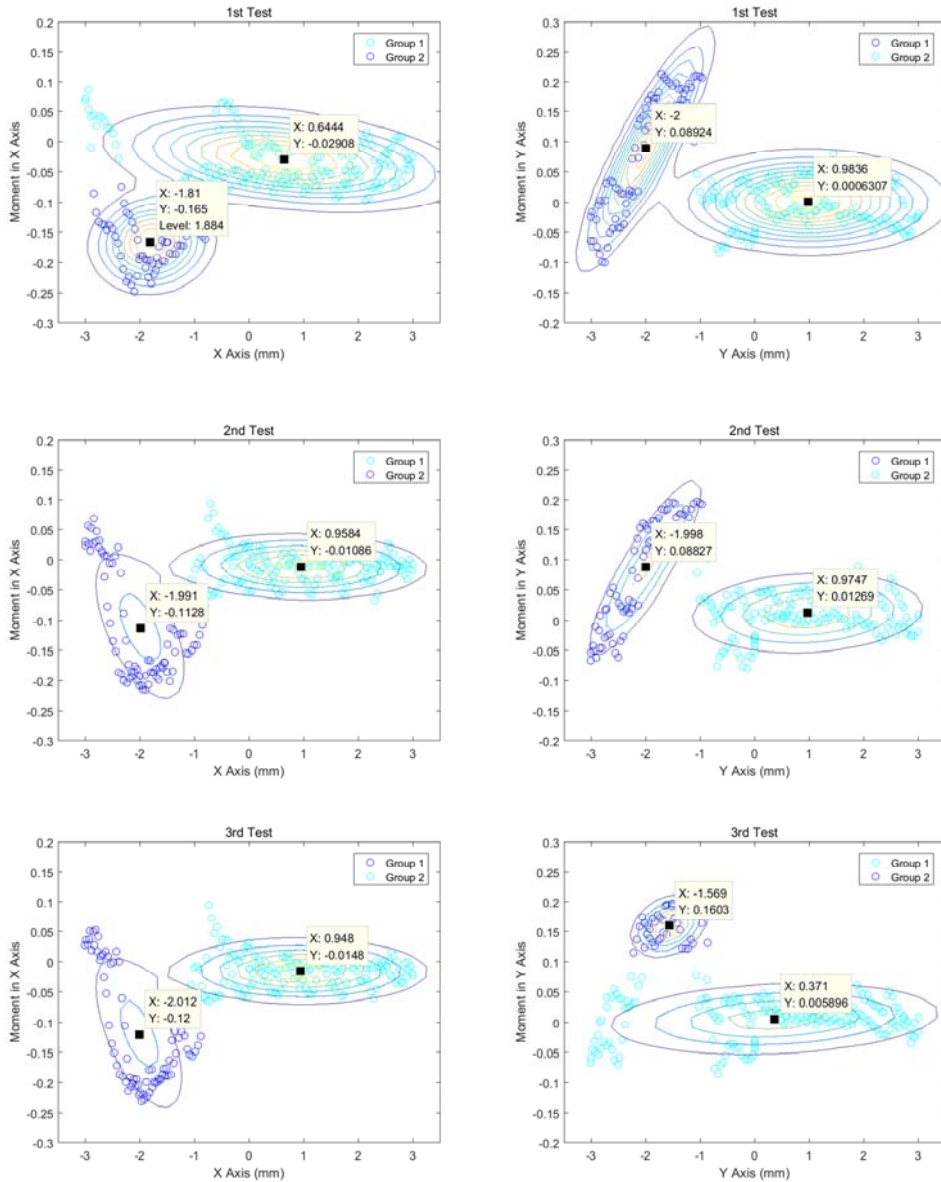


Figure 5.13 Clustering results with gaussian mixtue model algorithm on three datasets measured from same condition, Moment in x axis (Left), Moment in y axis(right)

This characteristics of covariance matrix influence on the accuracy of position error estimation significantly as shown in figure 5.13. It's clearly observed that the deviated results come out when the covariance matrix with strong relationship is assigned for the Gaussian distribution model. The covariance matrix with weak relationship, diagonal type, gives better results on error estimation and shows almost same result with K means cluster algorithm.

Table 5.6 Clustering results with gaussian mixtue model algorithm
on three datasets measured from same condition

| Test No | Position Error in X Axis | | | Position Error in Y Axis | | |
|-------------------|--------------------------|-------------|-------------------------|--------------------------|-------------|------------------------|
| | Number of Data | | Estimated Error (mm) | Number of Data | | Estimated Error(mm) |
| | Total | Cluster I | | Total | Cluster I | |
| 1 st | 245 | 66 (27%) | -1.810 | 245 | 82 (33%) | -2 |
| 2 nd | 247 | 80 (32%) | -1.991 | 247 | 82 (33%) | -1.998 |
| 3 rd | 246 | 79 (32%) | -2.012 | 246 | 47 (19%) | -1.569 |
| Average | 246 | 75 (30%) | -1.937 | 246 | 70 (28%) | -1.855 |
| Max difference | 2 | 14 | 0.202 | 2 | 35 | 0.431 |

The table 5.6 shows the summary of estimated position error and clustering results from Gaussian Mixture Model algorithm on the dataset in figure 5.13. The averaged position errors in x and y axis are -1.937mm and -1.855mm and maximum difference among three estimated position errors in x and y axis are 0.202mm and 0.431mm. After clustering the dataset to estimate the position error in x and y axis, different percentage of data in each dataset is assigned to the moment generated cluster depending on the covariance matrix. Among the 246 total data on average, the maximum difference on the number of data allocated to the moment generated cluster in each x and y axis is 14 and 35 respectively. The maximum error between estimated and given position error is 0.437mm. When the covariance matrix with weak relationship, diagonal type, is assigned for the Gaussian model, both of position error estimation and clustering results are almost same with those from K means clustering algorithm. However, when the covariance matrix with strong relationship between two joint variables is assigned for the Gaussian model, both of position error estimation and clustering results are different from those from K means clustering algorithm significantly. Therefore, it's verified that the accuracy of position error estimation from Gaussian Mixture Model algorithm depends on the characteristics of estimated model parameter, covariance matrix.

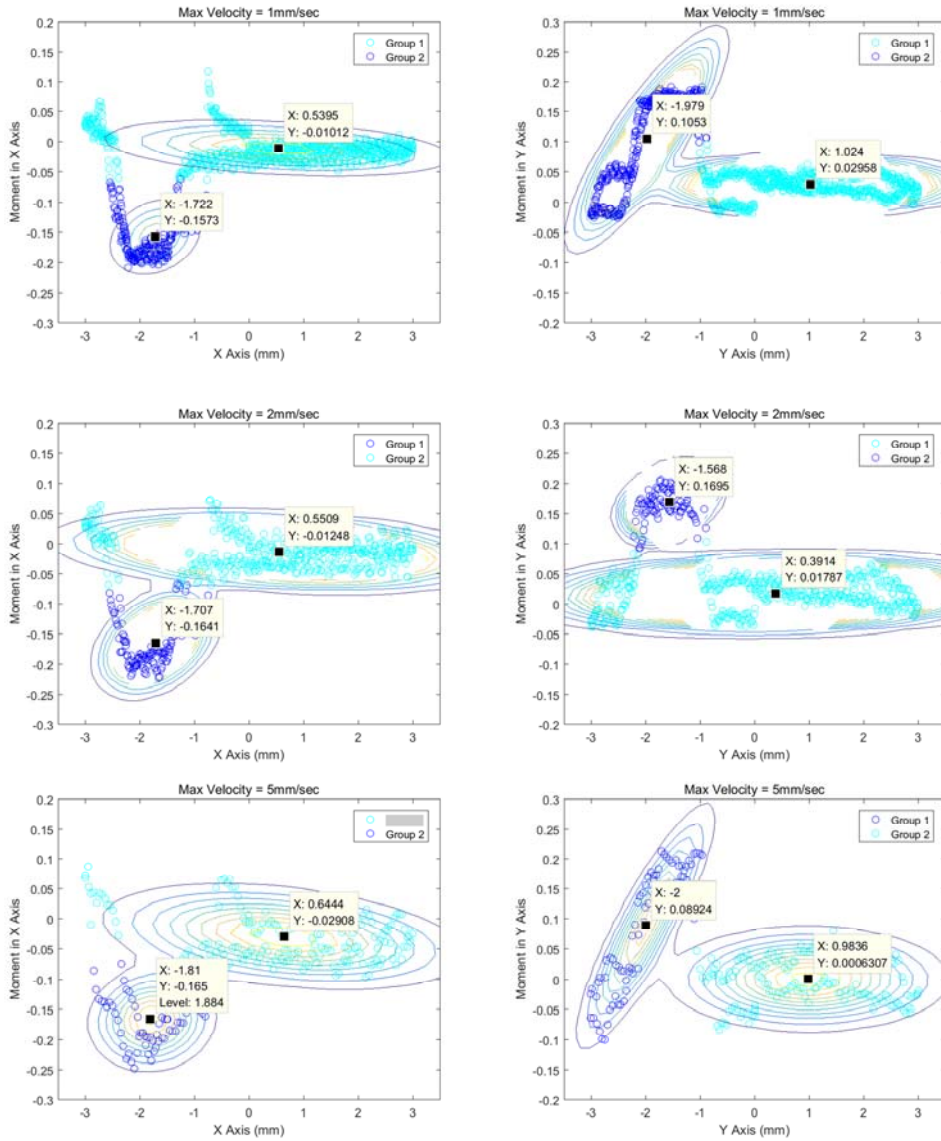


Figure 5.14 Clustering results with gaussian mixture model algorithm on three datasets measured from different velocity, 1mm/sec (Top), 2mm/sec (Middle), 5mm/sec(Bottom)

Applying Gaussian Mixture Model algorithm on the same dataset represented in figure 5. 11 which is measured with three different velocities, 1, 2 and 5 mm/sec, and given position error of 1.5mm in each axis, the clustered results for each dataset is indicated in figure 5.14. The same problems arisen from the dependency on the model parameter pointed out above still exists in error estimation regardless of the number of measured data in dataset.

Table 5.7 Clustering results with gaussian mixtue model algorithm
on three datasets measured from different velocity

| Velocity | Position Error in X Axis | | | Position Error in Y Axis | | |
|-------------------|--------------------------|--------------|-------------------------|--------------------------|--------------|-------------------------|
| | Number of Data | | Estimated Error (mm) | Number of Data | | Estimated Error (mm) |
| | Total | Cluster I | | Total | Cluster I | |
| 1mm/sec | 1,215 | 288 (24%) | -1.722 | 1,215 | 416 (34%) | -1.979 |
| 2mm/sec | 608 | 148 (24%) | -1.707 | 608 | 121 (20%) | -1.568 |
| 5mm/sec | 245 | 66 (27%) | -1.810 | 245 | 82 (33%) | -2 |
| Average | - | - | -1.746 | - | - | -1.849 |
| Max difference | - | - | 0.088 | - | - | 0.432 |

The table 5.7 shows the summary of estimated position error and clustering results from Gaussian Mixture Model algorithm on the dataset in figure 5.14. The averaged position errors in x and y axis are -1.746mm and -1.849mm and maximum difference among three estimated position errors in x and y axis are 0.088mm and 0.432mm. The maximum error between estimated and given position error is 0.349mm. In case of Gaussian model for position error estimation in x axis, the covariance matrix of diagonal type is used to model three dataset thus almost similar percentage, around 25%, of data is assigned to the moment generated cluster. In case of gaussian model for position error estimation in y axis, two different type of covariance matrix is used to model three dataset thus different percentage of data is assigned to the moment generated cluster. Therefore, it's verified that the accuracy and robustness of position error estimation from Gaussian Mixture Model algorithm does not depend on the number of data in dataset to represent the model but depends on the characteristics of model parameter, covariance matrix.

5.2.5 Comparison of clustering results

In summary, K means algorithm shows stable accuracy and robustness on position error estimation whereas the Gaussian Mixture Model algorithm needs to use constrained parameter for both of them. The two representative clustering algorithms are tested and verified with two datasets, one constructed with the three datasets

measured at same condition and the other constructed with three datasets measured with different velocity. The K means algorithm shows accuracy of estimated position error within 0.29mm and the deviation among each estimated error is within 0.14mm whereas the accuracy of estimated position error and deviation of that from Gaussian Mixture Model algorithm is 0.44mm and 0.43mm. The accuracy and robustness of error estimation from Gaussian Mixture Model algorithm mainly depend on the characteristics of parameter, covariance matrix, which determines the shape of distribution. However, the weakness from this dependency can be overcome by using constraint on type of covariance matrix. By assigning the diagonal covariance matrix which has no relationship between two joint variables, almost same results from K means algorithm can be acquired.

Both of clustering algorithms use optimization for clustering but the working principle inside of algorithm is different from each other. Therefore, this leads to different strength and weakness in clustering results. In case of K means clustering, it usually works very well but easily makes wrong clustering results even when there is one outlier in the dataset. In case of Gaussian Mixture Model algorithm, it's strong to the outlier in the dataset but dependency problem arisen from characteristics of parameter exists as described above. To overcome this, additional efforts for assigning the type of parameter for the expected clustering is necessary for good results. Considering these aspects, selective use depending on the distribution of data in dataset is required for the good clustering results in general.

Chapter 6

Conclusion

A lot of efforts have been made for robotic assembly by many researchers but Peg-In-Hole task, one of the simple and basic assembly tasks, is still challenging because accurate measurement and instantaneous judgement corresponding to the event is impossible to robot. Passive and active approaches stated above have strength and weakness in each of alignment method. The passive approach represented by RCC is only applicable to limited condition determined from chamfer size and length of peg. Active approaches based on vision also have limits on practical use because the accuracy of vision depends on installation location of camera and external environment significantly.

The force feedback during insertion is inevitable for damage prevention and efficient error estimation algorithm based on the force data measurement is required for error recovery. However, the solution for redundancy in force-torque map which make it hard to estimate the error from force and moment dataset is necessary for fast and robust recovery. The contact condition which determines the force-torque map is investigated and general analysis model for this is presented with connected component labeling. The contact conditions is defined with number of connected component and edge crossing peg and hole and reveals that moments are generated on only one of five cases in square Peg-In-Hole task. The fact that 3 cases originated from angular error distribute around target error position raise the need for angular error compensation through robust measurement.

For successful Peg-In-Hole, a dexterous gripper with an angular error measuring instrument and reliable error estimation algorithm which cluster position and moment dataset is proposed and tested with square Peg-In-Hole task. The proposed dexterous gripper makes it realized the use of finger for both of grasping and manipulation of peg. Fast and reliable error recovery is also achieved by angle measurement system,

scanner. The uncertainty in error estimation from redundancy in force-torque map, one of the main problems in error estimation, is solved with additional angle measurement.

The dexterous gripper which consists of 4 DOF(Degree Of Freedom) two fingers embedded with 6 axis force sensors at the fingertip is designed for micro manipulation of peg during error recovery. Different from the usual way, peg manipulation by robot arm and force measurement on the wrist, dexterous finger embedded with force sensors at the fingertip is designed and used for grasping and micro manipulating of peg. The optimized function for micro manipulation of peg, light weight around 1.5kg and small workspace with $\pm 5\text{mm}$ and $\pm 5\text{deg}$ in each axis, is implemented on the gripper and high position accuracy is achieved with ball screw actuation which has small lead, 0.635mm. The parallel mechanism is also implemented with combination of link and joint for fast dynamic characteristics of finger which is necessary for the task requiring interaction with environment.

The robust angle measurement instrument, scanner, consisted of 2DOF manipulator and laser distance sensor is also designed and implemented for detecting the angular error between peg and hole. The accuracy of scanner also depends on the frame structure the sensor mounted because the deflection of frame degrades sensor accuracy. The FEM model for deflection is generated with consistent mass and stiffness matrix and it's observed that sensor is deflected from $1.52\mu\text{m}$ to $17.64\mu\text{m}$ nonlinearly as it's positioned far away from origin. The calculated maximum straightness error and natural frequency of frame based on FEM model is $2.96\mu\text{m}$ and 270Hz. The accuracy of scanner is also verified through experiment which measures the angle of rotation stage. The measured accuracy of scanner is less than 0.1deg thus it's verified that scanner has enough accuracy and robustness in angle measurement.

Both of clustering algorithm, K means algorithm and Gaussian Mixture Model algorithm is applied to dataset constructed with the measured reaction moment and peg position data to estimate the position error between peg and hole. After categorizing the dataset into two clusters, moment generated or not, the center position in each of cluster is calculated and utilized for error estimation. To verify the accuracy and robustness of both algorithms, two datasets, one constructed with three datasets measured with same condition and the other constructed with three datasets measured

with different velocity are constructed and used for clustering algorithm. The K means algorithm shows accuracy of estimated position error within 0.29mm and the deviation among each estimated error is within 0.14mm whereas the accuracy of estimated position error and deviation of that from Gaussian Mixture Model algorithm is 0.44mm and 0.43mm. It's observed that the characteristics of parameter, covariance matrix, determine the accuracy and robustness of error estimation in Gaussian model based approach.

Comparing with blind search which usually uses no information from sensors and long spiral trajectory for error recovery, the proposed measurement system and error estimation algorithms have advantages in terms of shortened recovery time and no variation on recovery time. Short XY trajectory which moves horizontal and vertical line to cover given search area can be utilized to estimate error. The time for error recovery have no variation regardless of position error by diminishing the number of contact conditions through angular error measurement. In case of blind search which use spiral trajectory, the number of position to check for position error recovery in given square search area is proportional to squared number of steps, N^2 , whereas that of XY trajectory is proportional to $4N$. The variation of recovery time in blind search is proportional to N^2 depending on the position error whereas XY search has no variation on it.

In conclusion, the design of proposed gripper and scanner here is not only distinct but also useful for efficient error estimation based on the force measurement. The approaches attempted in this dissertation, contact condition analysis with connected component labeling and error estimation algorithm, are also applicable to other research area in robotic assembly thus expects to have excellent usability.

Bibliography

- [1] Daniel E. Whitney, "Mechanical Assemblies : Their Design, Manufacture, and Role in Product Development", Oxford Universe Press, 2004, pp. 263-287
- [2] Joo, Sangwan, Hiroyuki Waki, and Fumio Miyazaki. "On the mechanics of elastomer shear pads for remote center compliance (RCC)." *Robotics and Automation, 1996. Proceedings., 1996 IEEE International Conference on.* Vol. 1. IEEE, 1996.
- [3] Ciblak, Namik, and Harvey Lipkin. "New properties of the remote center of compliance." *Robotics and Automation, 1997. Proceedings., 1997 IEEE International Conference on.* Vol. 2. IEEE, 1997
- [4] Joo, Sangwan, and Fumio Miyazaki. "Development of variable RCC and its application." *Intelligent Robots and Systems, 1998. Proceedings., 1998 IEEE/RSJ International Conference on.* Vol. 2. IEEE, 1998.
- [5] Zhao, Fuliang, and Paul SY Wu. "VRCC: A variable remote center compliance device." *Mechatronics* 8.6 (1998): 657-672.
- [6] Lee, Sangcheol, Sangchul Won, and Seungjoon Choi. "Development of a new variable remote center compliance for assembly robots." *Advanced Robotics* 14.3 (2000): 241-255.
- [7] Lee, Sangcheol. "Development of a new variable remote center compliance (VRCC) with modified elastomer shear pad (ESP) for robot assembly." *IEEE Transactions on Automation Science and Engineering* 2.2 (2005): 193-197.
- [8] Bright, G., and C. Deubler. "Design and implementation of an intelligent Remote Centre Compliance (IRCC) as a means of intelligent position feedback for a construction robot." *IAARC/IFAC/IEEE. International symposium.* 1999.
- [9] Cheng, Chi-Cheng, and C. H. E. N. Gin-Shan. "A Multiple RCC device for polygonal peg insertion." *JSME International Journal Series C Mechanical Systems, Machine Elements and Manufacturing* 45.1 (2002): 306-315.
- [10] Ciblak, Namik, and Harvey Lipkin. "Design and analysis of remote center of compliance structures." *Journal of Field Robotics* 20.8 (2003): 415-427.
- [11] Lee, Sangcheol. "Shear control of elastomer shear pads for variable remote center compliance." *Advanced Robotics* 23.1-2 (2009): 227-237.
- [12] Havlik, Š. "Passive compliant mechanisms for robotic (micro) devices." *13th World Congress in Mechanism and Machine Science, Guanajuato, Mexico.* 2011.

- [13] Chhatpar, Siddharth R., and Michael S. Branicky. "Search strategies for peg-in-hole assemblies with position uncertainty." *Intelligent Robots and Systems, 2001. Proceedings. 2001 IEEE/RSJ International Conference on*. Vol. 3. IEEE, 2001.
- [14] Park, Hyeonjun, et al. "Intuitive peg-in-hole assembly strategy with a compliant manipulator." *Robotics (ISR), 2013 44th International Symposium on*. IEEE, 2013.
- [15] Huang, Jian, Toshio Fukuda, and Takayuki Matsuno. "Model-based intelligent fault detection and diagnosis for mating electric connectors in robotic wiring harness assembly systems." *IEEE/ASME Transactions on Mechatronics* 13.1 (2008): 86-94.
- [16] Chen, Fei, et al. "A Study on Error Recovery Search Strategies of Electronic Connector Mating for Robotic Fault-Tolerant Assembly." *Journal of Intelligent & Robotic Systems* 81.2 (2016): 257-271.
- [17] Dietrich, Franz, et al. "Enhancements of force-torque map based assembly applied to parallel robots." *Industrial Technology (ICIT), 2010 IEEE International Conference on*. IEEE, 2010.
- [18] Dietrich, Franz, et al. "On contact models for assembly tasks: Experimental investigation beyond the peg-in-hole problem on the example of force-torque maps." *Intelligent Robots and Systems (IROS), 2010 IEEE/RSJ International Conference on*. IEEE, 2010.
- [19] Kim, Young-Loul, Byeong-Sang Kim, and Jae-Bok Song. "Hole detection algorithm for square peg-in-hole using force-based shape recognition." *Automation Science and Engineering (CASE), 2012 IEEE International Conference on*. IEEE, 2012.
- [20] Kim, Young-Loul, Hee-Chan Song, and Jae-Bok Song. "Hole detection algorithm for chamferless square peg-in-hole based on shape recognition using F/T sensor." *International journal of precision engineering and manufacturing* 15.3 (2014): 425-432.
- [21] Song, Hee-Chan, Young-Loul Kim, and Jae-Bok Song. "Guidance algorithm for complex-shape peg-in-hole strategy based on geometrical information and force control." *Advanced Robotics* 30.8 (2016): 552-563.
- [22] Peña-Cabrera, Mario, et al. "Machine vision approach for robotic assembly." *Assembly Automation* 25.3 (2005): 204-216.
- [23] Wang, Junping, and Hyungsuck Cho. "Micropeg and hole alignment using image moments based visual servoing method." *IEEE Transactions on Industrial Electronics* 55.3 (2008): 1286-1294.

- [24] Chang, R. J., C. Y. Lin, and P. S. Lin. "Visual-based automation of peg-in-hole microassembly process." *Journal of Manufacturing Science and Engineering* 133.4 (2011): 041015.
- [25] Huang, Shouren, et al. "Fast peg-and-hole alignment using visual compliance." *Intelligent Robots and Systems (IROS), 2013 IEEE/RSJ International Conference on*. IEEE, 2013.
- [26] Pauli, Josef, Arne Schmidt, and Gerald Sommer. "Servoing mechanisms for peg-in-hole assembly operations." *International Workshop on Robot Vision*. Springer Berlin Heidelberg, 2001.
- [27] Jain, Ravi K., Somajoyti Majumder, and Ashish Dutta. "SCARA based peg-in-hole assembly using compliant IPMC micro gripper." *Robotics and Autonomous Systems* 61.3 (2013): 297-311.
- [28] Feng, Chen, et al. "Vision guided autonomous robotic assembly and as-built scanning on unstructured construction sites." *Automation in Construction* 59 (2015): 128-138.
- [29] Di, Pei, et al. "Hybrid vision-force guided fault tolerant robotic assembly for electric connectors." *Micro-NanoMechatronics and Human Science, 2009. MHS 2009. International Symposium on*. IEEE, 2009.
- [30] Stemmer, Andreas, et al. "Robust assembly of complex shaped planar parts using vision and force." *Multisensor Fusion and Integration for Intelligent Systems, 2006 IEEE International Conference on*. IEEE, 2006.
- [31] Mezouar, Youcef, Mario Prats, and Philippe Martinet. "External hybrid vision/force control." *Intl. Conference on Advanced Robotics (ICAR07)*. 2007.
- [32] Thomas, Ulrike, et al. "Multi sensor fusion in robot assembly using particle filters." *Robotics and Automation, 2007 IEEE International Conference on*. IEEE, 2007.
- [33] Haraguchi, Rintaro, et al. "Development of production robot system that can assemble products with cable and connector." *Journal of Robotics and Mechatronics* 23.6 (2011): 939-950.
- [34] Chen, Fei, et al. "i-hand: An intelligent robotic hand for fast and accurate assembly in electronic manufacturing." *Robotics and Automation (ICRA), 2012 IEEE International Conference on*. IEEE, 2012.
- [35] Stemmer, Andreas, A. Albu-Schaffer, and Gerd Hirzinger. "An analytical method for the planning of robust assembly tasks of complex shaped planar parts." *Robotics and Automation, 2007 IEEE International Conference on*. IEEE, 2007.

- [36] Song, Hee-Chan, Young-Loul Kim, and Jae-Bok Song. "Automated guidance of peg-in-hole assembly tasks for complex-shaped parts." *Intelligent Robots and Systems (IROS 2014), 2014 IEEE/RSJ International Conference on*. IEEE, 2014.
- [37] Grana, Costantino, Daniele Borghesani, and Rita Cucchiara. "Connected component labeling techniques on modern architectures." *Image Analysis and Processing-ICIAP 2009* (2009): 816-824.
- [38] Schwenk, Kurt, and Felix Huber. "Connected Component Labeling algorithm for very complex and high-resolution images on an FPGA platform." *SPIE Remote Sensing*. International Society for Optics and Photonics, 2015.
- [39] C.M. Bishop, "Pattern Recognition and Machine Learning", Springer, 2006, pp. 423-439

Abstract in Korean

펙인홀(Peg-In-Hole) 작업은 로봇을 활용한 조립작업 중 가장 기초적인 작업이라고 할 수 있다. 조그마한 위치 에러에도 끼임 현상(Jamming 또는 Wedging)이 발생하고 이는 부품 삽입 중에 파손을 유발할 수 있기 때문에, 조립 대상물간의 위치 및 방향에 대한 정렬이 성공적인 펙인홀 작업을 위해서는 무엇보다 중요하다. 이러한 펙인홀 작업을 위해서는 지금까지 많은 연구가 진행되어 왔으며, 대상물간의 정렬 방식에 따라서 수동적 또는 능동적 방법으로 구분된다. RCC(Remote Center Compliance)로 대표되는 수동적인 정렬방법은 컴플라이언스와 대상 부품의 특정 모양을 이용하는 반면에, 능동적인 정렬방법은 비전이나 조립 시 발생하는 반력 정보를 이용하여 대상물간의 정렬을 수행한다. 수동적 정렬 방법은 특별한 측정이나 노력 없이 사용될 수 있다는 장점을 가지고 있지만, 부품의 챔버(Chamfer) 사이즈나 펙의 길이 등에 따라서 사용 가능 여부가 결정되어 적용이 제한적이다. 비전의 활용을 통한 정렬도 또한 적용이 제한적인데, 그 이유는 카메라의 설치 위치 및 주변 환경에 따른 측정 정확도의 민감성 때문이다.

본 학위 논문에서는 효과적인 펙인홀 작업을 수행하기 위하여 다자유도의 그리퍼, 각도 에러 측정기 및 측정된 힘 정보를 군집화하여 대상물간의 위치 에러를 측정할 수 있는 알고리즘이 제안되었다. 이를 위하여 하단의 주요 세가지 핵심 기능이 시스템 설계에 구현되었으며, 사각 형상의 펙인홀 작업을 통해 증명되었다.

위치 에러 보정 작업 시 미세 조정 작업을 위하여, 4 자유도를 지닌 두 개의 손가락으로 구성된 그리퍼가 설계되었으며, 손가락 끝 단에는 6축 힘 센서가 내재되어 반력 측정을 가능하게 하였다. 로봇의 손목에 설치된 힘 센서와 로봇 팔의 자유도를 사용하여 작업을 수행하는 일반적인 방법과는 달리, 설계된 다자유도 그리퍼를 활용하여 펙을 조작 가능하게 하였다. 또한, 펙의 양 측면에서 발생된 반력 정보들을 펙의 위치 정보와 함께 저장하여 위치에러 도출에 활용 가능하도록 하였다.

2 자유도의 직교 로봇과 레이저 거리 센서로 구성된 견실한 각도 측정기(Scanner)가 펙과 홀 사이의 각도 에러 보정을 위하여 설계 및 구현되었다. 펙과 홀 사이의 접촉 조건에 따라서 모멘트 반력의 발생 유무가 결정되는데, 힘 정보를 바탕

으로 한 빠르고 신뢰성 있는 에러 추정을 위해서는 각도 에러 측정을 통한 보정을 필요로 한다. 사각형상의 펙 인 홀 작업의 경우에는, 펙과 홀 사이의 엣지 및 지지 면의 수에 따라서 총 5가지의 경우로 접촉 조건이 분류가 되는데, 모멘트는 그 중에서 한가지의 경우에만 발생하게 된다. 각도 에러 보정을 통하여, 접촉 조건은 2가지로 줄어들게 되며, 이를 통하여 에러 보정 시간을 줄이는 것이 가능하다.

펙과 홀 사이의 위치 에러를 추출하기 위하여, 모멘트 반력 정보와 펙의 위치 정보로 구성된 데이터 세트에 군집화 알고리즘을 적용하였다. 각도 에러 보정 후에도, 모멘트가 발생하지 않는 경우가 남게 되며 이러한 혼합된 데이터 세트에서도 위치 에러를 추출할 수 있는 인공지능을 필요로 한다. 이를 위하여, 기계 학습에서 사용되는 두 가지의 대표적인 알고리즘, K 평균 알고리즘과 가우시안 혼합 모델 알고리즘을 다양한 측정 데이터 세트들에 적용하였다. 에러 추출 시 알고리즘의 정확도와 견실함을 확인 하기 위하여 같은 조건에서 측정되거나 다른 속도에서 측정된 세 개의 데이터 세트가 위치 에러 추출을 위하여 사용되었다. K 평균 알고리즘의 경우, 추출된 위치 에러의 정확도와 각각의 데이터 세트에서 추출된 위치 에러 값들의 편차는 각각 0.29mm, 0.14mm 이내이지만, 가우시안 혼합 모델 알고리즘의 경우에는 각각 0.44mm, 0.43mm를 보이고 있다. K 평균 알고리즘은 위치 에러 추출에서 안정적인 정확도와 견실함을 가지며, 가우시안 혼합 모델 알고리즘은 위하여 제한조건을 지닌 파라미터 사용을 필요로 하는 것을 확인할 수 있다.

센서로부터의 정보에 의지하지 않고, 긴 나선형 궤적만을 이용하여 에러 보정을 수행하는 블라인드 서치(Blind Search)와 비교할 때, 제안된 측정기와 위치 추출 알고리즘은 짧고 편차가 없는 에러 보정 시간의 장점을 가지고 있다. 주어진 검색 영역을 수직 수평으로 움직이는 짧은 XY 궤적을 사용하여 에러 보정 시간을 단축 가능하게 하고, 각도 에러 보정을 통하여 접촉 조건 경우의 수를 줄이면서 에러 보정을 위한 시간에 편차가 없도록 하였다.

주요어 : 로봇을 활용한 조립, 펙 인 홀 작업, 에러 보정 알고리즘, 블라인드 탐색, 지능 탐색, 다자유도 그리퍼

학번 : 2014-30339